X-460-70-386
PREPRINT

NASA TM X- 65401

PERFORMANCE OF ATS SPIN-SCAN CLOUDCOVER CAMERA (SSCC) EQUIPMENT AT MOJAVE GROUND STATION

OCTOBER 1970

GSFC
GODDARD SPACE FLIGHT CENTER
GREENBELT, MARYLAND

14

X-460-70-386

PERFORMANCE OF ATS SPIN-SCAN CLOUDCOVER CAMERA (SSCC) EQUIPMENT AT MOJAVE GROUND STATION

ATS Project

October 1970

GODDARD SPACE FLIGHT CENTER
Greenbelt, Maryland

The text of this document, compiled for the ATS Project by the Documentation Branch, Technical Information Division, GSFC, originated in material supplied by Westinghouse Electric Corporation under contract NAS-5-10217 and by the University of Wisconsin.

CONTENTS

ILLUSTRATIONS

ILLUSTRATIONS (continued)

TABLES

PERFORMANCE OF ATS SPIN-SCAN CLOUDCOVER CAMERA (SSCC) EQUIPMENT AT MOJAVE GROUND STATION

INTRODUCTION

This document presents the results of an evaluation of spin-scan cloudcover equipment used for the ATS-1 at the Mojave, California, ground data-acquisition station. The equipment investigated included the phase-lock loop (PLL), the video subsystem, the photofacsimile subsystem, and the digital recording subsystem.

Investigation of the PLL included an analysis of an optimal tracker and compared its performance with the observed performance of the Mojave PLL. The study compared optimum values for PLL smoothing constants, obtained from analysis of a theoretical model, with optimum values obtained by direct experimentation.

The study of the video subsystem ranged from the spacecraft to the inputs of the various recorders, with emphasis on noise, bandwidth, and linearity. This report describes anomalies observed during the first year of operation (such as video streaking and sun flare) and includes recommendations for improving performance.

The report on performance of the film recorder used with the SSCC describes the modulation-transfer function (MTF) and its relation to the level of intensity. The areas of study defined there provide a basis for modifying existing recorders or for developing future film recorders.

The discussion of the digital recording subsystem includes a brief history of the operational difficulties experienced, and a detailed analysis of a typical data tape.

PERFORMANCE OF THE PHASE-LOCK LOOP

Objectives of this analysis were to compare the actual performance of the sun-pulse tracking system with that of a theoretically optimum system, and to recommend improvements where possible.

The tracking system performs two independent operations: pulse detection and smoothing. The filter-threshold detector does the pulse detection, and the phase-lock loop (PLL) does the smoothing. The analysis of the pulse-detection problem compares an optimum detector with the actual detector used in the system; if the filter time constant and the threshold level are suitably chosen, the actual detector's performance is within a factor of 2 of that of the theoretical detector.

Next, after setting up a noise and spin-acceleration model for spacecraft data by assuming the form of the model, then finding parameters of the optimum filter that will separate these two components, the filter parameters will serve to calculate the model parameters. Comparison of the optimum filter and the PLL, using a computer simulation of the PLL, indicates that the PLL is virtually as good as a second-order optimum filter. Changing the frequency and phase-correction settings of the simulated PLL produced optimum results that closely agree with those of the onsite tests.

Appendix A contains the detailed mathematical procedures used in setting up the theoretical model and in calculating the optimum threshold level and sync error variances used in the comparisons.

VIDEO SUBSYSTEM PERFORMANCE

Evaluation of the performance of the SSCC video-processing subsystem resulted in several recommendations for improved equipment performance.

Tests to investigate the characteristics of the video-processing system with regard to noise, frequency response, and amplitude linearity used a specially built test device, the RF switch, which has four inputs: 70 MHz; (70 + X) MHz; a switching rate, R_s; and a logic-control line. If the logic-control input is 1, then the output of the RF switch changes between 70 MHz and (70 + X) MHz at a rate R_s; if the logic-control input is 0, then the output of the device is 70 MHz.

Linearity

Measurements of amplitude linearity covered only two areas, one being the FM discriminator characteristics and the other the linearity of the entire ground equipment from the FM discriminator to the video-processor output buffers. Linearity was investigated for signals whose FM deviation ranged up to 10 MHz; as the maximum deviation from the spacecraft is less than 10 MHz in wideband data mode 2, this range appeared to be adequate.

Figure 1 is a plot of FM discriminator output versus intermediate frequency representing the characteristic curve of the discriminator for Mojave. The curve is the result of static tests using an RF-signal generator as the IF source and measuring the corresponding dc output of the generator. For purposes of this report, deviation from linearity (in percent) is the root mean square (rms) of the departures from the least-squares fit, divided by full-scale times 100. The Mojave discriminator shows excellent linearity over the range of expected deviations.

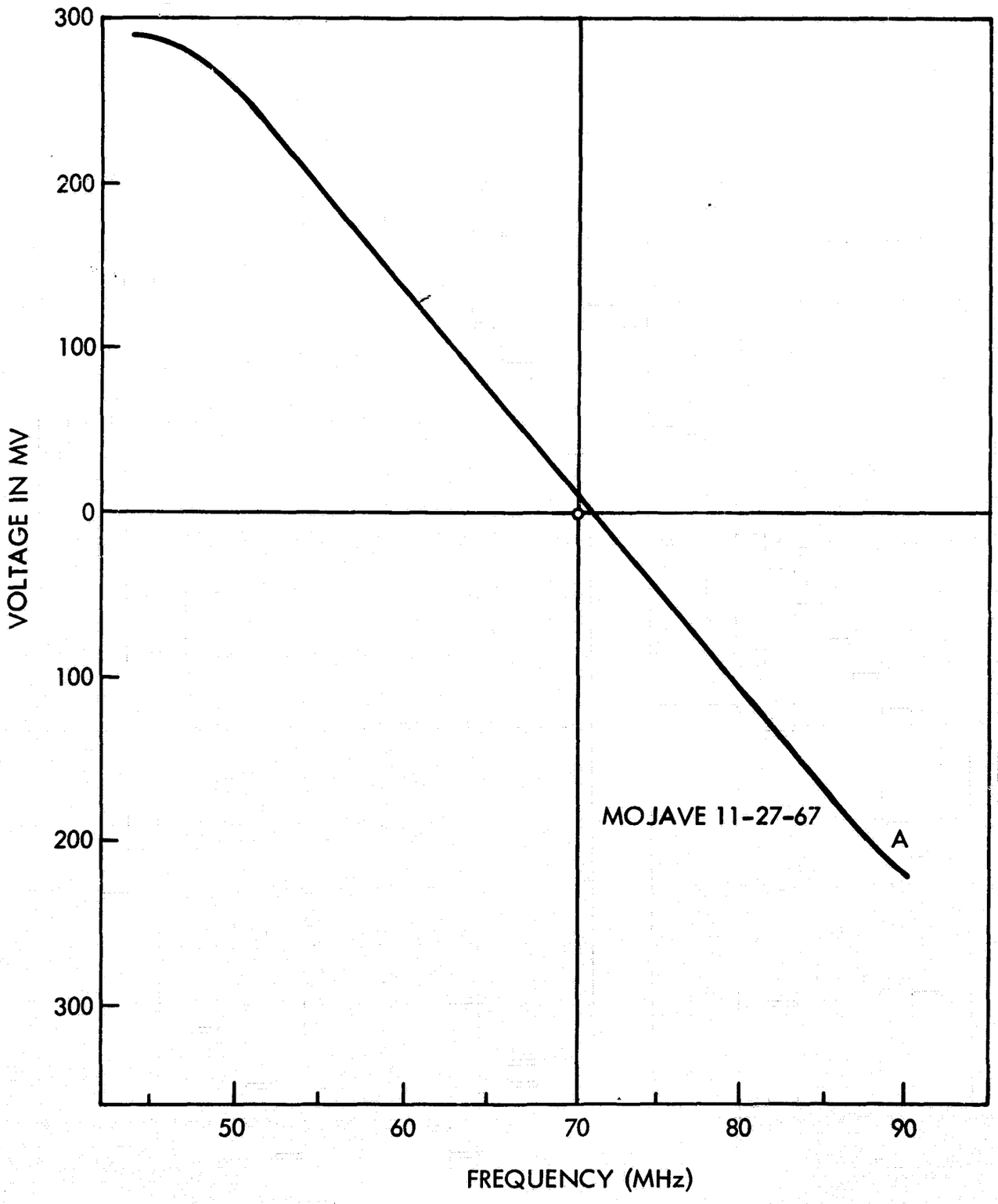

Figure 1. FM Discriminator Output vs IF Frequency

The tests of video-system linearity used the RF switch to avoid any influence on the data from the linearity characteristics of an FM modulator. The output of the RF switch, when demodulated, is a squarewave with amplitude proportional to X and with repetition rate R_s. This waveform is present only during the time that PEP-enable is a logic 1, ensuring that the test signal has a duty cycle similar to that of the camera signal and that the timing is correct with respect to the dc-restore pulse.

Figure 2 is a plot of the amplitude of the output-buffer signal versus X, the FM deviation. The FM deviation was incremented in 1-MHz steps. The signal amplitude was measured at the digital output buffer (curve A) and the photofax output buffer (curve B) was recorded for each step. The two curves represent least-squares fits to the data points. The ground equipment appears to be linear within 2.7 percent for the digital buffer output, and within 3.3 percent for the photofax buffer output. As the video system is common up to the input of the output buffers and the two buffer amplifiers are identical circuits, the differences in the linearity measurements probably represent errors in measuring. If this is true, the uncertainty in the linearity measurements is of the order of 1 percent. The linearity test does show that the gain of the photofax buffer was low by 5 percent and that of the digital buffer by 10 percent.

Frequency Response

Investigation of the ground equipment's frequency response covered two domains. High-frequency response characteristics were investigated by passing a squarewave test signal from the RF switch through the video processor and noting any distortion. This test was repeated for square waves with repetition rates of 5, 10, 20, and 40 kHz. For this test, the FM deviation (X) was set to 5 MHz.

Figure 3 is a photograph of the output of the preemphasis network at a repetition rate of 5 kHz; the slight asymmetry of the waveform is due to misalignment of the zero-crossing detector in the RF switch, not to the video-processing system. Figure 4, a photograph of the same waveform at the output of the 200-kHz filter input card, shows some ringing. (Note that the sweep in all these pictures is from right to left.) Figure 5 is a photograph of the same output as it appears at the digital buffer; the absence of visible degradation between the latter two figures indicates that, at the 5-kHz rate, the only degradation of the video signal is the ringing introduced by the 200-kHz filter. Repetition of the test at 10 and 20 kHz produced essentially the same results. Figure 6 is a photograph of the output of the preemphasis network at R_s = 40 kHz; the signal shows no degradation. Figure 7 shows that, at the output of the 200-kHz filter, the repetition rate of the test video is so fast that the ringing never has a chance to decay. This distortion, propagated without change through the rest of the video system, appears at the output of the digital buffer as shown in Figure 8.

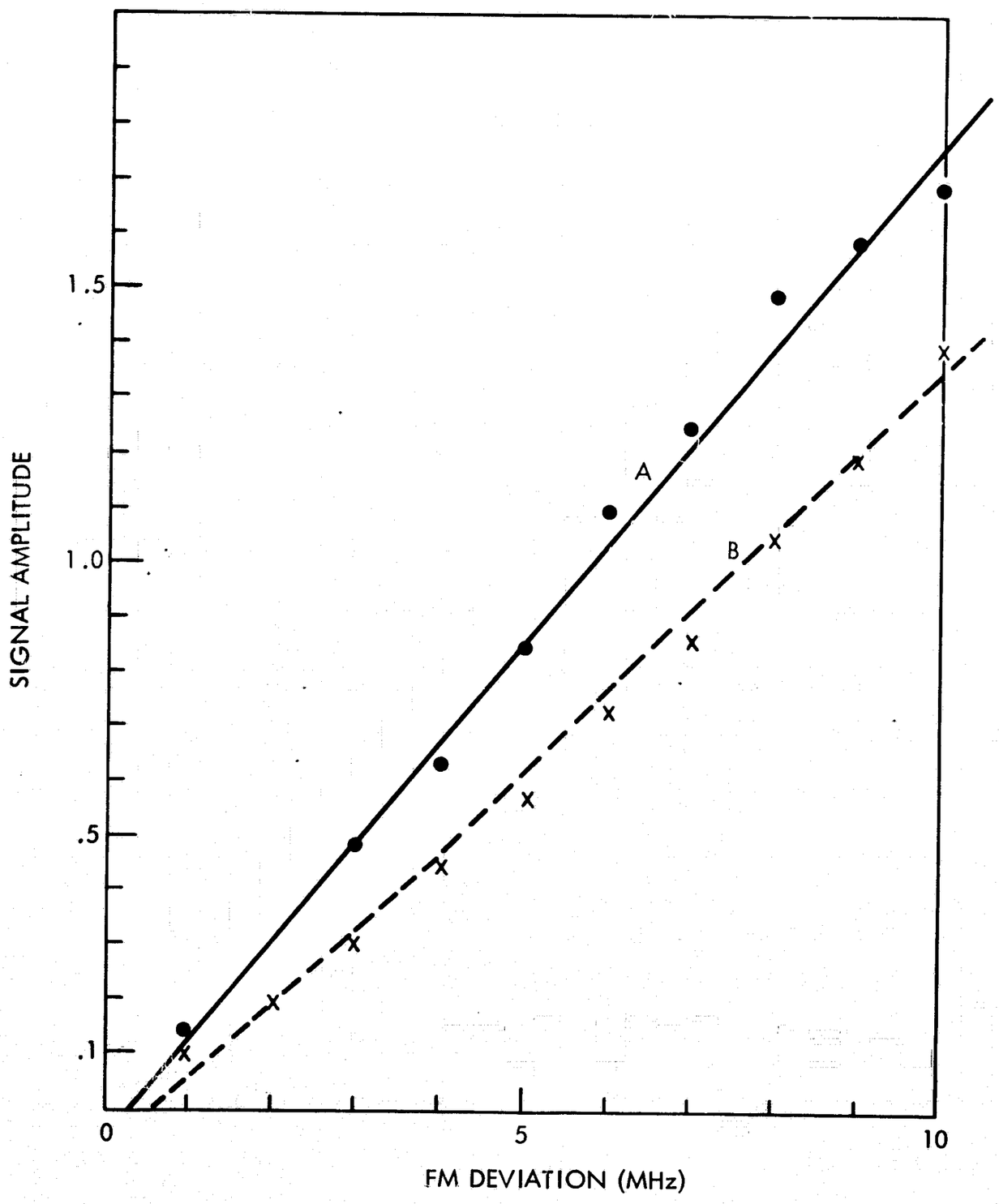

Figure 2. Output Buffer Signal vs FM Deviation (X)

.1 ms/cm

.5 v/cm

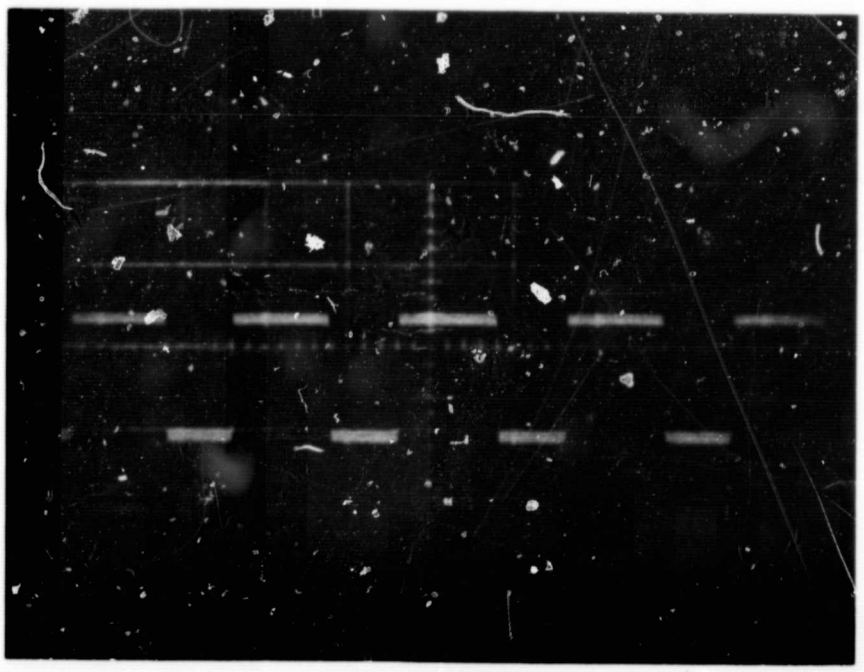

Figure 3. Output of Preemphasis Network (R_s = 5 kHz)

.2 ms/cm

.5 v/cm

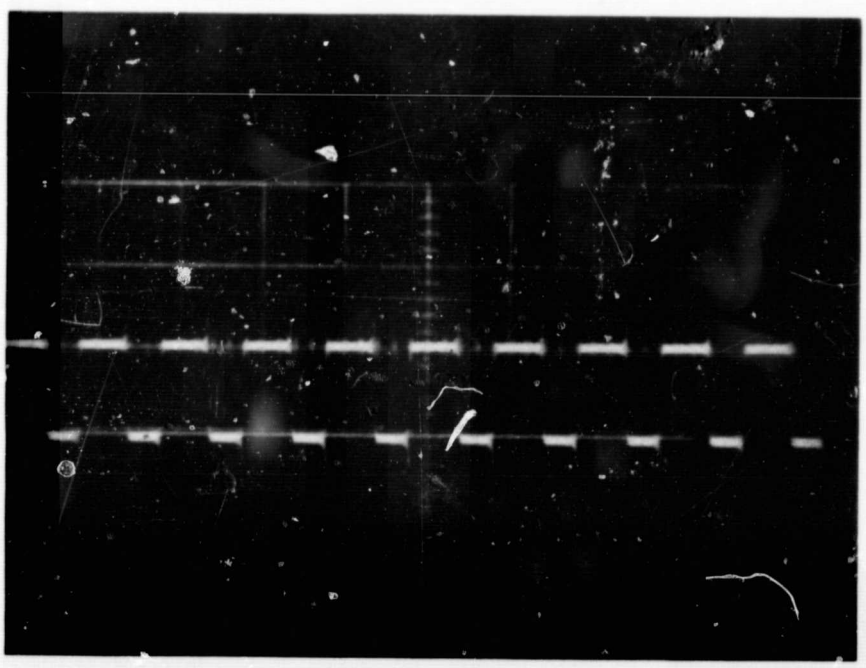

Figure 4. Output of 200-kHz Filter (R_s = 5 kHz)

.2 ms/cm

.5 v/cm

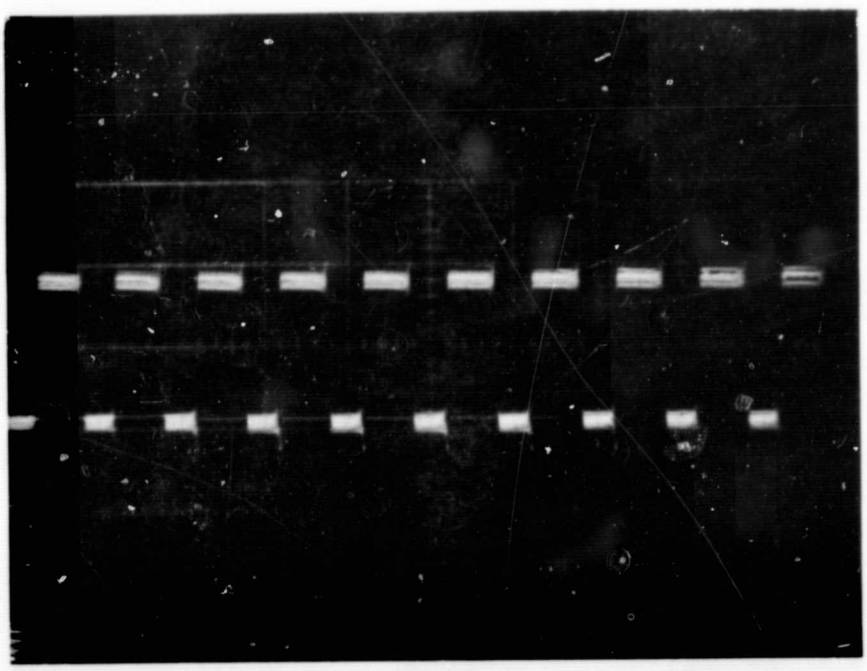

Figure 5. Output of Digital Buffer (R_s = 5 kHz)

20 μs/cm

.5 v/cm

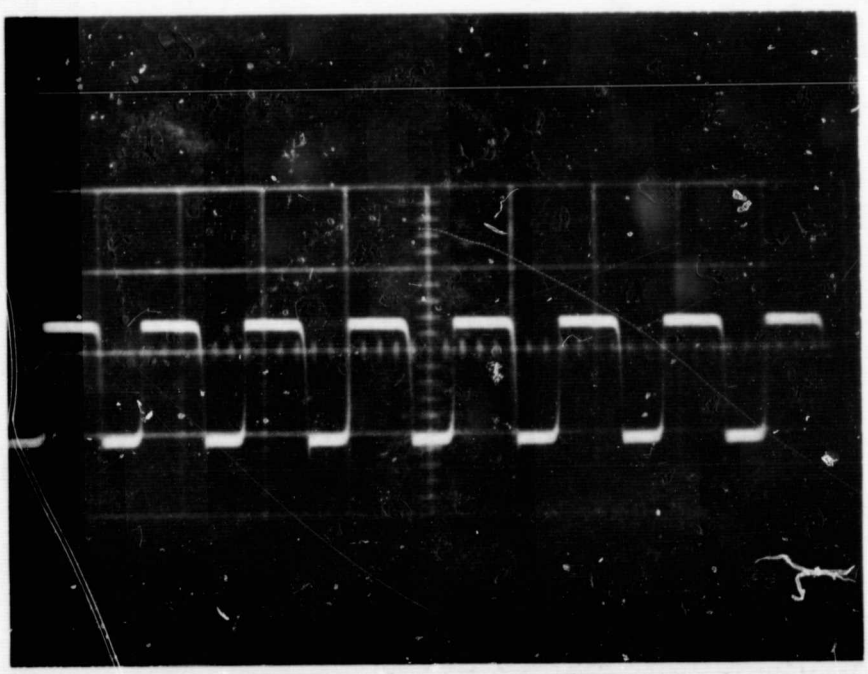

Figure 6. Output of Preemphasis Network (R_s = 40 kHz)

20 μs/cm

.5 v/cm

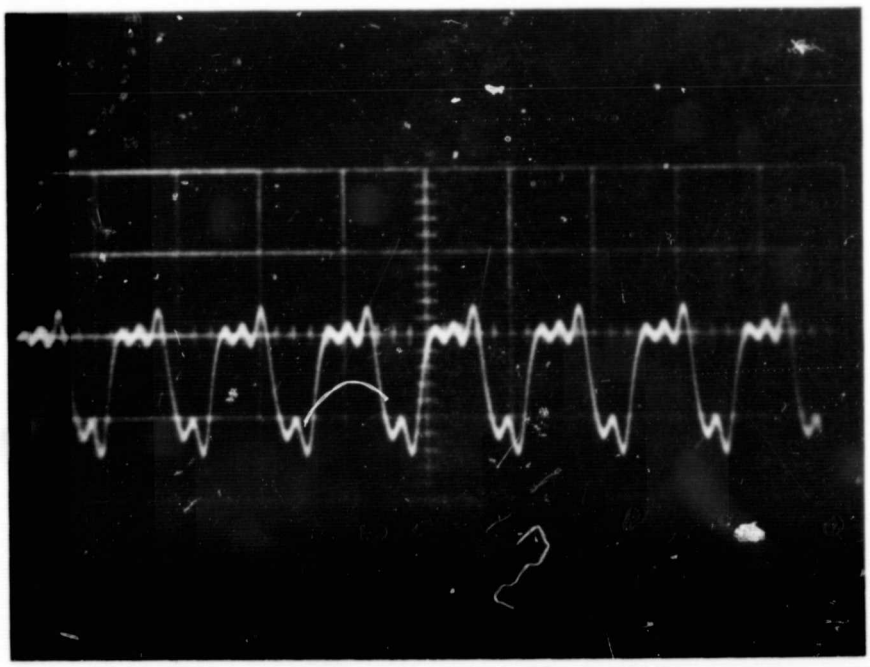

Figure 7. Output of 200-kHz Filter (R_s = 40 kHz)

20 μs/cm

.5 v/cm

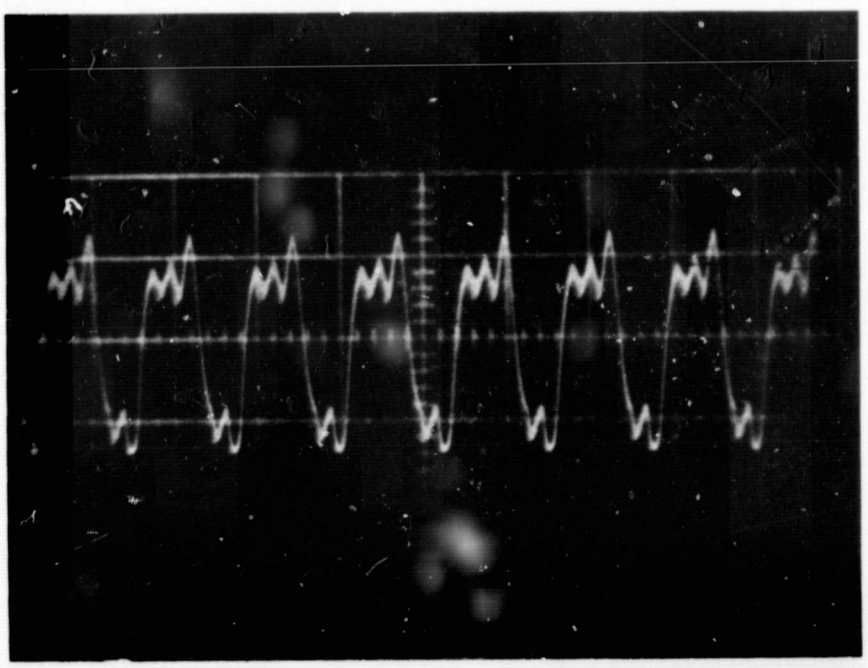

Figure 8. Output of Digital Buffer (R_s = 40 kHz)

The overshoot and ringing seen in these pictures corresponds to a filter-damping ratio of 0.27 with a resonant frequency of 200 kHz. This underdamped characteristic of the filter is responsible for distorting the test signal.

The frequency response of this filter indicates an increasing gain up to 200 kHz: at 50 kHz, the gain is high by about 1 db, at 100 kHz it is high by about 2 db, and at 200 kHz it rises to about 7 db. The fact that the data content above 50 kHz is small means that signal distortion is small.

The RF switch also served for testing the low-frequency response of the video system. When the switching rate R_s is removed as an input to the RF switch, the logic-control line controls the RF switching. If PEP-enable is a logic 1, the output of the RF switch is 75 MHz; when it is a logic 0, the output is 70 MHz. When this output is demodulated, the resulting signal is a 30-ms flat-topped pulse which completely fills the SSCC data window; degradation (tilt) of this pulse was the criterion for evaluating low-frequency response characteristics of the video. The test was performed both with and without the preemphasis network included in the circuit.

Figure 9 is a photograph of the receiver mod output showing no discernible tilt. Figure 10 is a photograph of the same waveform at the digital buffer output; any tilt that exists is too small to be measured from these scope photographs. Comparison of the two photographs shows that the video system without the preemphasis network can pass a square pulse whose width is equal to the data window, with no measurable tilt.

The test just described took place in January 1968 after the system had been in the field for about a year. During this time, the video system underwent two modifications to improve low-frequency response: When the system was installed, the coupling capacitors located at the receiver-modification input, the separator input, and the dc-restore input had values of 150 microfarads each. The receiver-modification output was coupled into the preemphasis network with three 150-mf capacitors in parallel. Also, in March 1967, the aforementioned coupling capacitors (except for those in the preemphasis network) were replaced by 540-mf capacitors.

Installation of the 540-mf capacitors produced a dc drift in the video processor output that saturated the video signal, resulting in severe distortion. The conclusion was that the low-frequency gain of the preemphasis network was enhancing the drift. If the drift occurred at a frequency of 0.01 to 0.1 Hz at the receiver discriminator, the net gain would be 20 (receiver mod) times 30 (preemphasis), or approximately 600; thus, a drift of half a millivolt at the receiver-discriminator output would provide the observed 300 mv at the video-processor input card. Maximum drift allowable at the latter card without degrading system performance is on the order of 100 mv.

5 ms/cm

.5 v/cm

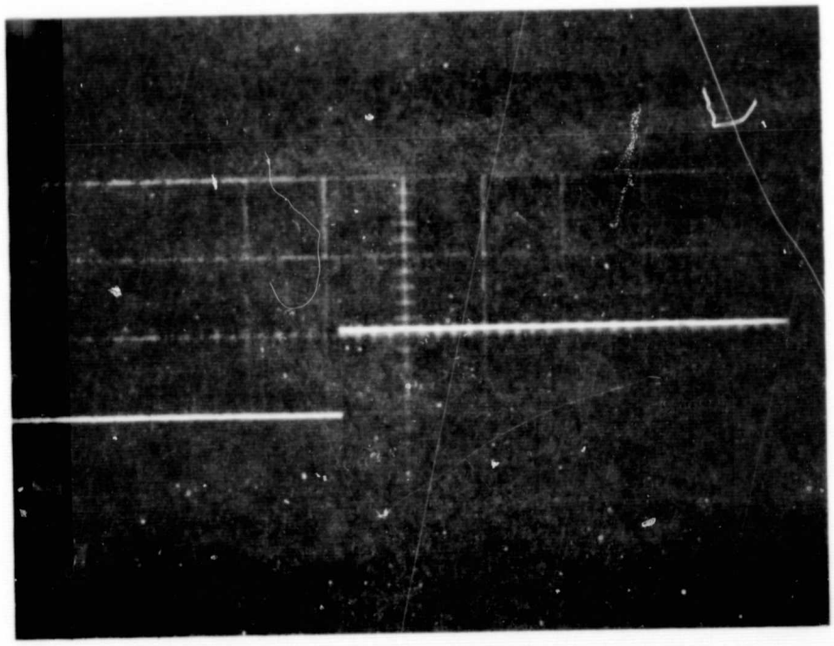

Figure 9. Receiver Modification Output

5 ms/cm

.5 v/cm

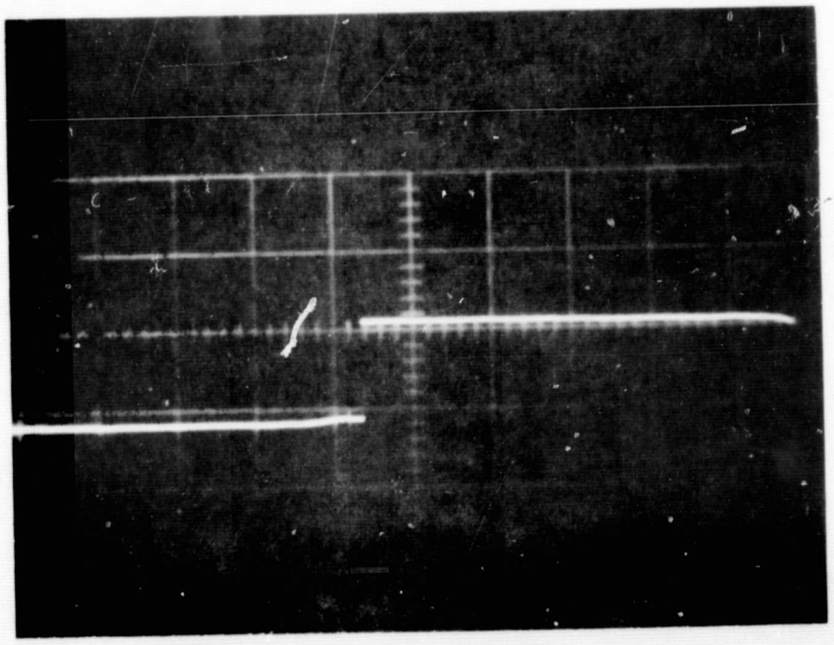

Figure 10. Digital Buffer Output

Replacement of the 540-mf capacitor at the input to the receiver-modification amplifier with a 150-mf capacitor reduced the drift to less than 20 mv, well below the threshold for video degradation. A new wideband receiver-mod amplifier installed at Mojave in early January of 1968 has presented no difficulties; the 330-mf coupling capacitor on the input of this receiver mod will probably be the final configuration.

Shortly after the beginning of spacecraft operations, a preemphasis network was installed between the receiver-mod amplifier and the video processor in order to correct for insufficient low-frequency response in the spacecraft. The signal droop caused by the spacecraft electronics for a given video signal was computed, and the effect of the preemphasis network was calculated using step and frequency-response methods. Finally, the effect of the preemphasis network on a typical spacecraft signal was checked. Appendix B contains a description of these procedures.

Noise

System noise tests to determine the amounts and types of noise introduced by the video-processing portion of the SSCC equipment comprised three types of measurement: The first was to determine the amount of wideband noise present at different points in the system; the second, to ascertain the composition of the wideband noise previously measured; and the third, to determine the amount of dc offset at various points in the system.

Wideband noise was measured with an HP 3400A true rms voltmeter bridged into the video-processing system at six points. During these measurements, the input to the receiver-mod amplifier was grounded in order to remove the influence of the unquieted FM receiver. As the voltmeter had a wide bandwidth (15 MHz), the effective noise (200 kHz) was much less than indicated. Noise levels measured, in millivolts, were:

Receiver-mod amplifier output	9.2
Preemphasis network output	14.0
Photofax buffer A3TP1	9.7
Digital buffer A4TP1	9.1
Microwave buffer A4TP3	13.0
Analog recorder buffer A3TP3	17.5

A Tektronics 585A oscilloscope with a type D plug having a sensitivity of 1 mv/cm served to measure dc offset at six points in the video-processing system.

The dc level was within ±5 mv of ground level; some cases required a prior adjustment.

Anomalies

When operating in wideband mode 1, a very high video level (such as bright white cloud) causes the video signal to momentarily drive to a high level and then recover. This phenomenon has appeared in both the earth video and the sun flare when it occurs. As a result of this condition, photographs taken in wideband mode 1 exhibit "black holes" in what ought to be the brightest area of the white cloud. When the sun flare shows this overload condition, it appears as a spurious sun pulse approximately 3 degrees away from the true sun pulse; this has, on occasion, caused the phase-lock loop to drop lock. Tests conducted to determine what part of the system was causing this overload revealed that the signal from the receiver-mod amplifier showed the overload condition. Further investigations of the problem have therefore been confined to the SHF receiver area.

Figure 11 is a diagram of the test setup used to check out the receiver-disc-amplifier system under high-level input signals. The SSCC calibration pulse through attenuators A and B drove the 70-MHz test modulator. Figure 12 shows the discriminator output and the corresponding modulator output as viewed on a spectrum analyzer, for three levels of input. The two top photographs are typical of the two signals under normal conditions; the middle photographs show the effect of a decrease of 0.6 db in attenuator B (the output of the FM modulator is distorted, with a new peak in the spectrum at 54 MHz; the output of the discriminator is beginning to change its polarity); and the lower photographs show the results of another 0.2-db increase in attenuator B. The new peak in the IF spectrum is present, and the discriminator output has completely reversed its polarity. The spectrum-analyzer photographs indicate that driving the FM modulator beyond its limits is causing the 54-MHz peak; the discriminator reacts to this change by driving to a positive level. This test shows that, when the test modulator is overdriven, the output contains frequencies that correspond to a signal of the opposite polarity.

In the wideband mode 1 configuration, the input to the FM modulator in the spacecraft is 10 db greater than in the wideband mode 2 normally used. If the spacecraft modulator reacts to very high-level input signals as the test modulator does, then the obvious result will be video-signal inversion at very high levels. Further work should be done on characteristics of the spacecraft modulator.

Another problem since the beginning of spacecraft operations has been persistent video streaking. Two independent sources of this streaking have been evident, one associated with the spacecraft and the other associated with the ground equipment.

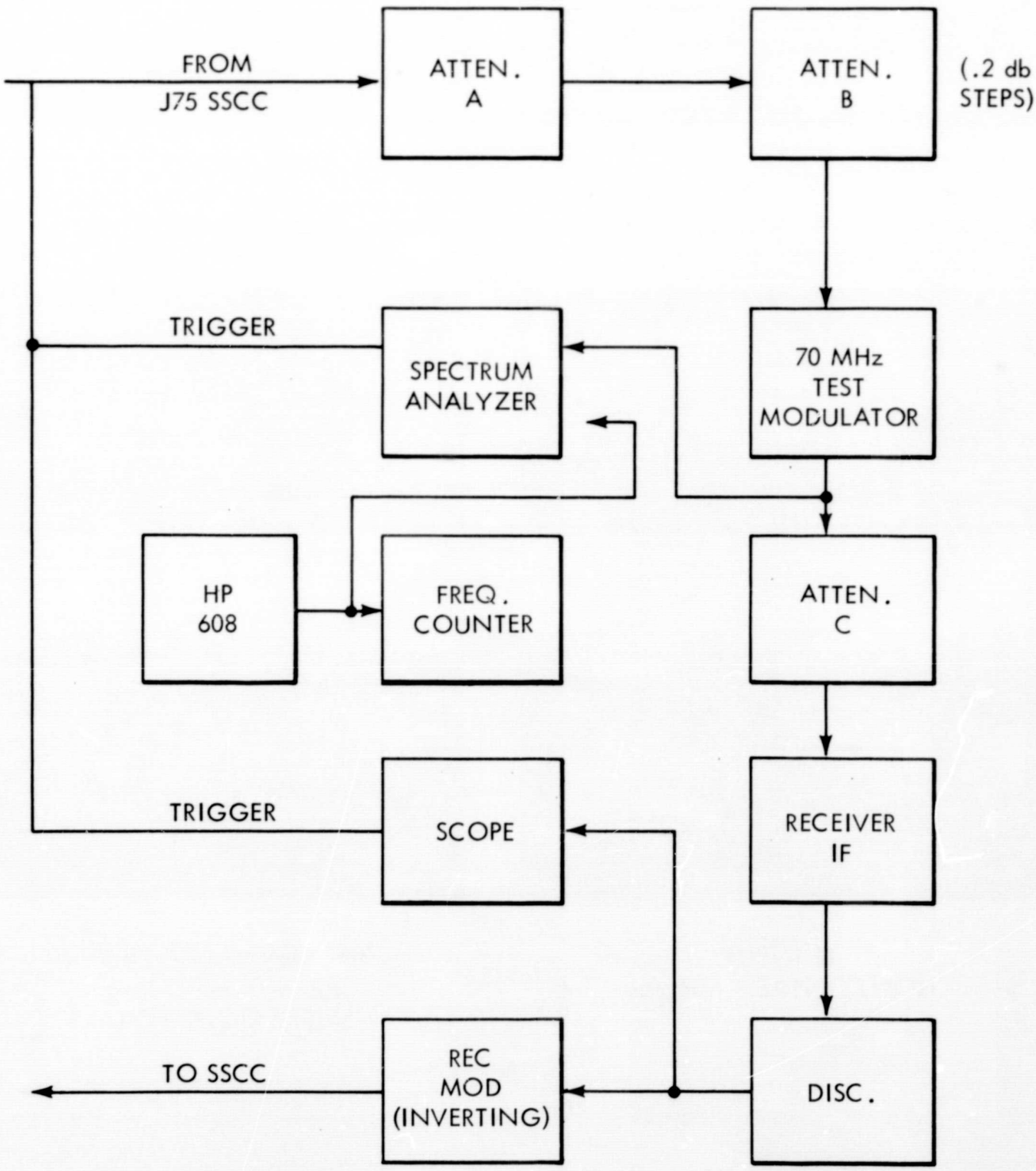

Figure 11. Overload Test Setup

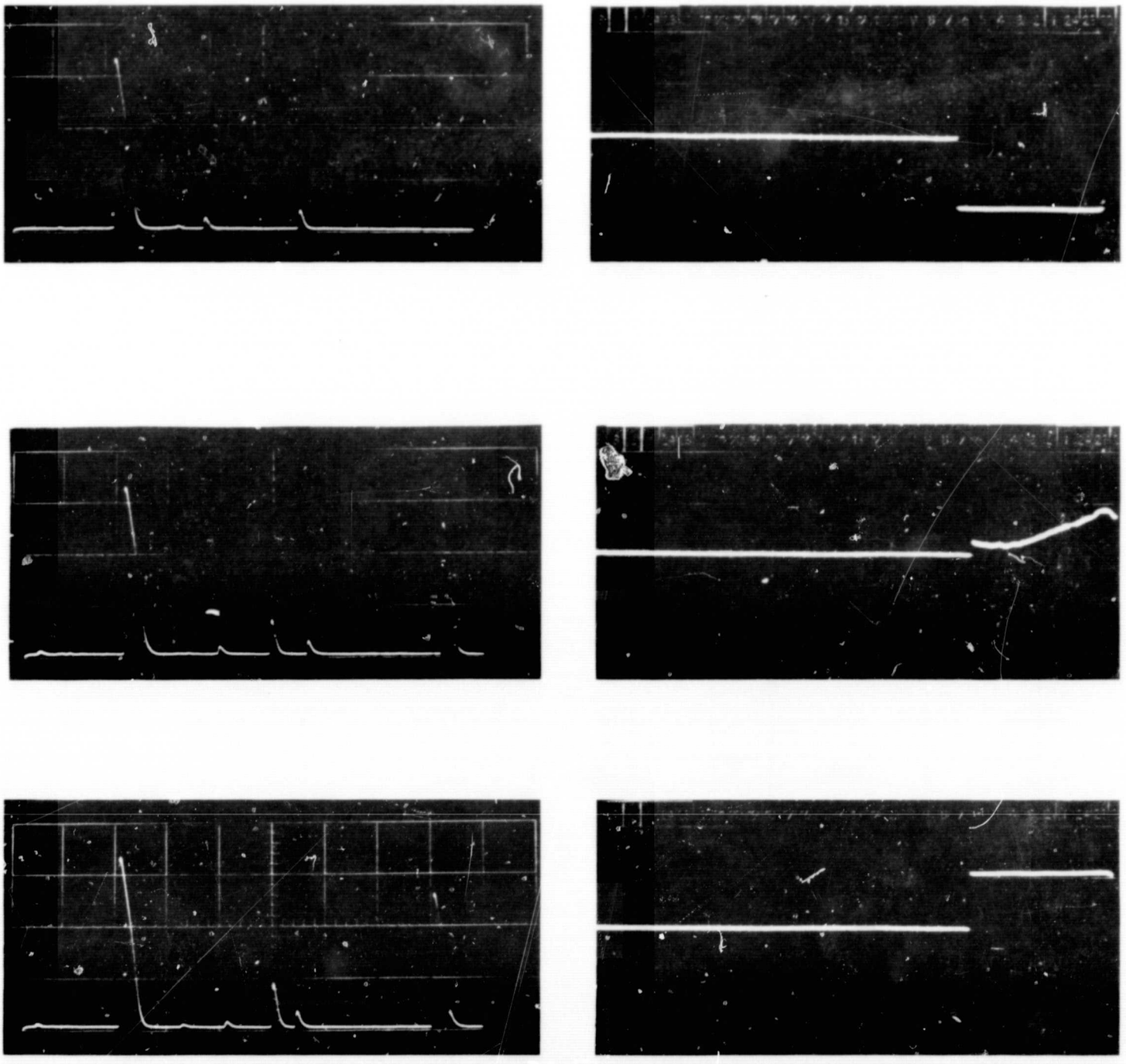

IF INPUT
HORIZONTAL 6 MHz/cm

DISCRIMINATOR OUTPUT
100 mv/cm - 2 ms/cm
SWEEP RIGHT TO LEFT

Figure 12. Spectrum-Analyzer View of Discriminator and Corresponding Modulator Output

On days 159 and 160 in 1967, several pictures exhibited severe streaking caused by a line-to-line shift in the video baseline. Figure 13 is an example of this type of streaking. The VHF regulator was on almost continuously during this period of time, resulting in low voltage of the battery bus. On day 160, an experiment to investigate possible correlation between this type of streaking and the use of the VHF regulator under low battery-bus voltage resulted in the pictures shown here as Figure 14. The first is a photograph of the SSCC video taken while the VHF regulator was on; note the extra large pulse. This picture, 160 M2, was badly streaked. During picture 160 M3, the VHF regulator was turned off and the picture shows no streaking. Immediately thereafter, the VHF regulator was turned back on and the resulting waveform appears as the third picture. This test makes it clear that the combination of low battery voltage and the use of the VHF regulator seriously distorts the video signal from the spacecraft, and this distortion results in streaking of the SSCC pictures. In almost a year of operation, this type of streaking has occurred during only one time period, day 159 and 160, so that it is not a major problem. Avoiding the circumstances that caused this distortion should prevent its recurrence.

Besides the VHF streaking, the SSCC pictures have exhibited the type of distortion shown in the three photographs of Figure 15. Interference of this sort, an

Figure 13. VHF Regulator-Related Streaking

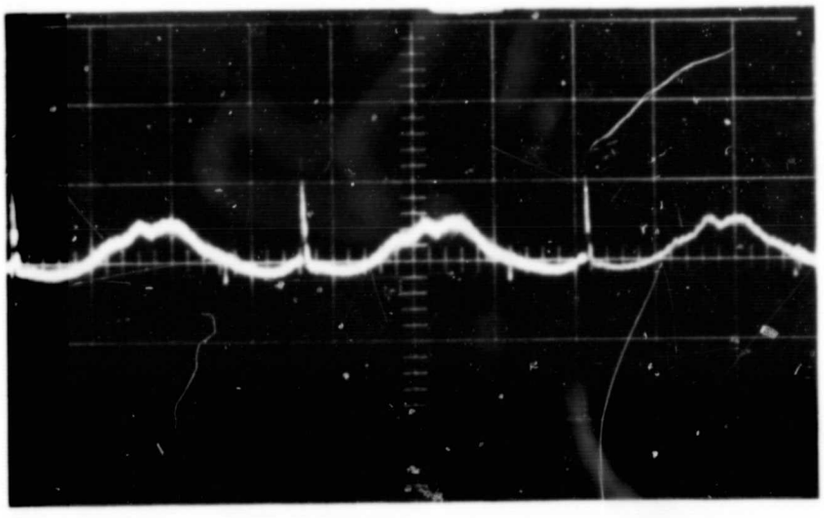

(A)

1 VOLT/cm

170 ms/cm

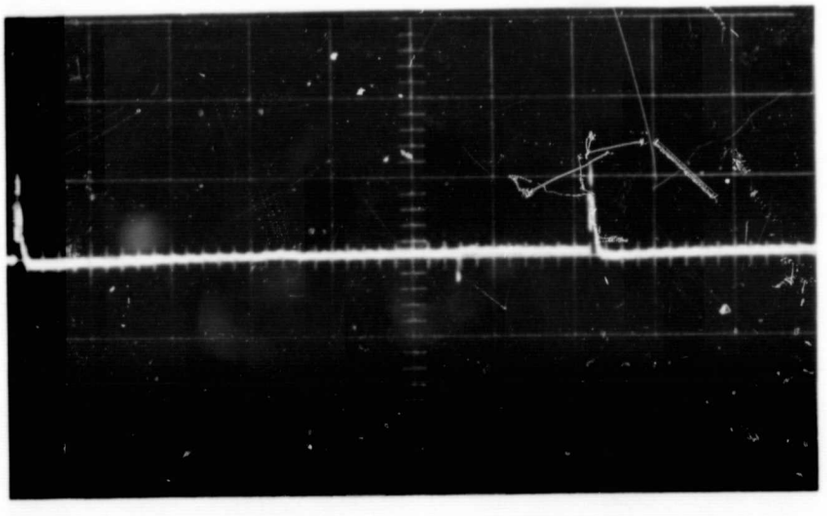

(B)

1 VOLT/cm

85 ms/cm

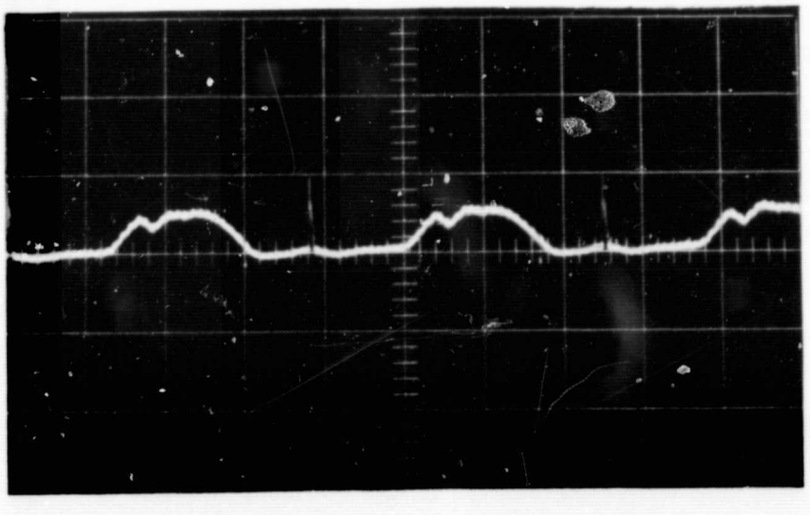

(C)

1 VOLT/cm

170 ms/cm

Figure 14. VHF Streak

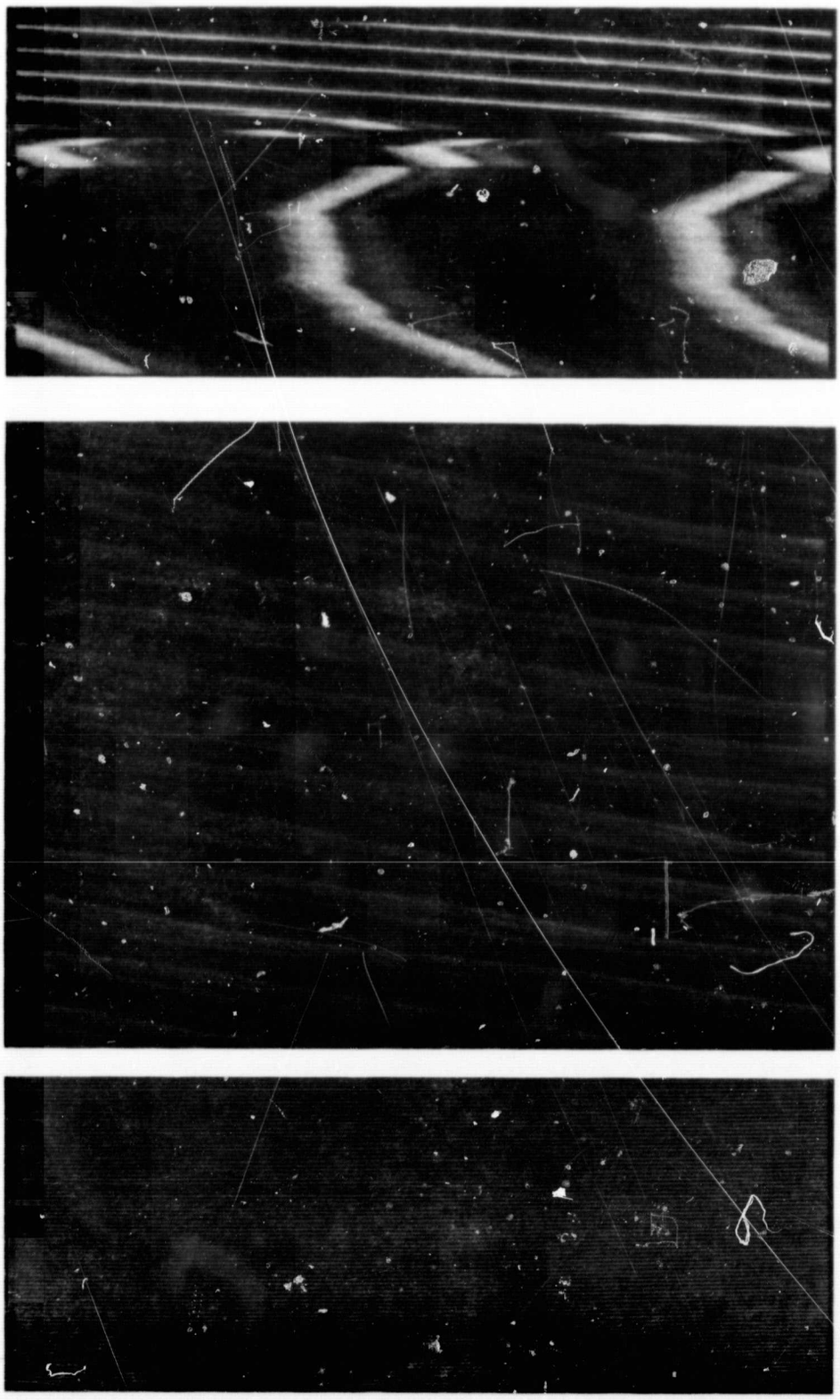

Figure 15. Video Streaking

intermittent problem since picture-taking began, results from interaction between the VCO frequency and the low-level 60-cycle noise. The photographs in Figure 15, taken with 12-db ground-station gain, were printed in such a way as to enhance the hum bars. Interference levels this high have never appeared on an earth picture. Changes in the VCO frequency will cause the streaks to change width and angle with respect to the horizontal, and at times to disappear. When the spin period is close to a multiple of 16 2/3 ms, the streaks become broad and angled; when this condition does not exist, the streaks become horizontal and narrow, so that they tend to merge and cause an apparent increase in the base density of the negative. The narrow horizontal condition of the streaks is the one most usually observed.

Investigation has shown that the low-level 60-cycle noise is already present in the receiver-mod amplifier output, and that the video processor itself does not add 60-cycle noise to the signal.

In June 1967, an effort to clean up existing ground loops at Mojave was partially successful; the source of the 60-cycle hum appeared at that time to be the grounding system. The 60-cycle interference has not presented a major problem since that time.

For about 5 weeks at the time of the equinox, the spacecraft camera (as well as the sun sensor) is able to "see" the sun; during this time, the video picture will include a region where both the camera and the regular sun sensor see the sun. As the two sensors respond with signals of opposite polarity that are algebraically summed in the satellite, and the two are approximately 3 degrees apart, the negative-going sun pulse will go above ground, as shown in Figure 16.

The flare-control circuit receives its input from the output of the video-processor input card. When the flare-control switch in the logic rack enables this circuit, the video signal remains clamped to zero at all times except when the sun-pulse time gate is a logical true (i. e., the line is released when the sun pulse is expected). The waveform of Figure 16 thus becomes that of Figure 17, which replaces the normal sun pulse from the separator.

The difficulty encountered in keeping the sychronizer in phase lock, even with the new clamp circuit, results from the difference between the voltage peak of the clamp-circuit output and the actual voltage peak of the sun pulse, the system timing being a function of that peak. One way to improve the existing circuit would be to increase the resolution (gain) of the clamp-circuit output in order to keep the inherent error more uniform from one line to the next.

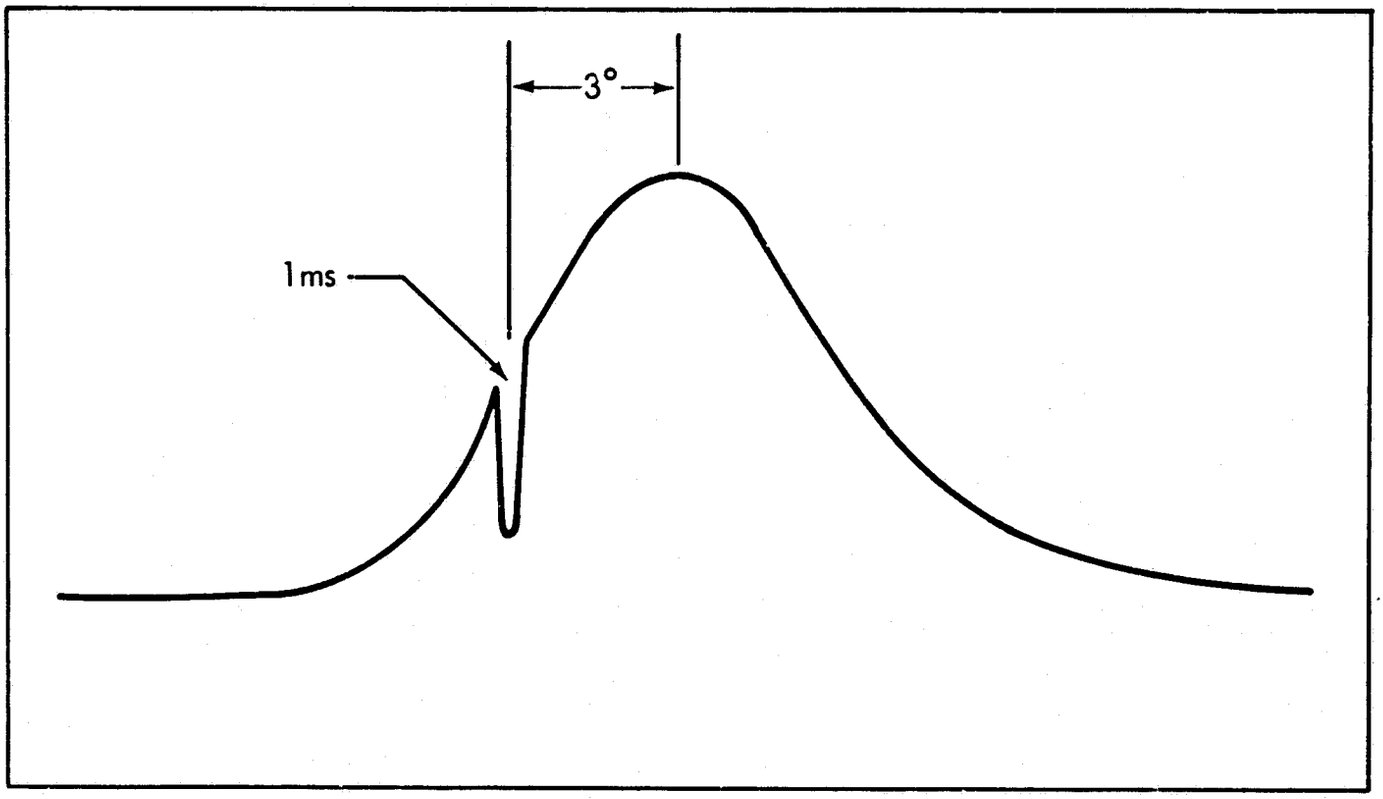

Figure 16. Flare Unit Input

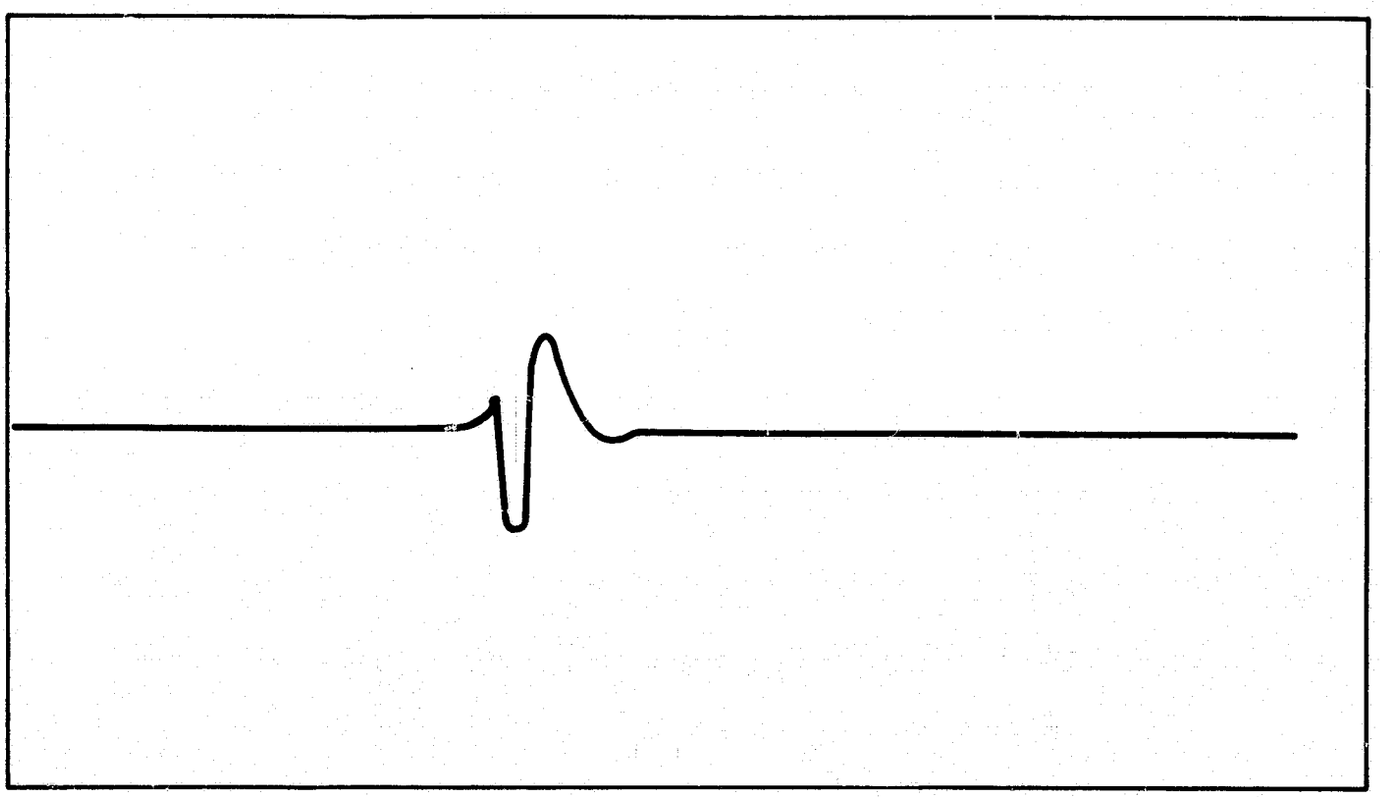

Figure 17. Flare Unit Output

Possible System Improvements

The 200-kHz filter (an eight-section low-pass filter with Chebyshev response) appears to cause some video degradation. The electrical characteristics of this filter should be changed from a Chebyshev to a Butterworth response because the Chebyshev function is relatively unsatisfactory for pulse or video applications, owing to the ripples in its amplitude range and its poorer phase characteristics. This type of application requires a filter response such as the Butterworth which exhibits a small overshoot and good phase characteristics. Changing the parameters of the existing Chebyshev to a Butterworth response by changing the values of the circuit components in the present filter will eliminate the necessity of completely redesigning the printed circuit card.

The input to the preemphasis network should be changed to a differential input, or a differential -1 amplifier should be installed at Mojave. This change would significantly reduce the present 60-cycle interference in the SSCC video, as the primary source of this interference is pickup along the lengthy cable between the receiver and the SSCC equipment. Addition of an expanded-portion playback feature at Mojave is an incentive for changing the preemphasis to differential input, because any 60-cycle interference that does exist is more apparent in expanded playback.

The bandwidth of the buffers should be reduced. At present, the -3-db point of the output buffers is about 5 MHz; as the SSCC video contains little if any information above 150 kHz, this extra bandwidth acts only to pass along high-frequency noise, mostly from the central timing unit. Narrowing the bandwidth to the limits of the video signal will improve the signal-to-noise ratio of the video signal.

The flare circuit is not completely successful in its operation, not because of any defect in the circuit but rather because of the difficulty of extracting a signal in the presence of large noise (flare). During periods of moderate to large interference, turning off the flare circuit will remove the sun pulse from the phase-lock loop. Use of the VCO-dot option should result in little drift of the picture position. Experience in using this technique should lead to an effective operational procedure.

PHOTOFAX SUBSYSTEM PERFORMANCE

In May 1968, the film recorder used as part of the SSCC equipment at the Mojave STADAN site was evaluated in order to see how it performed after installation of a new cathode-ray tube (P24). The evaluation found that the recorder had inadequate resolution and needed adjustment to improve its performance. Additional performance tests were made for varying beam currents and lens openings,

for open versus closed loop operation, and with and without yellow filters in the optical path.

After the initial adjustment of the recorder, only one difficulty appeared: an intermittent 500-kHz oscillation on the output of both deflection amplifiers, after 4 days of tests, caused severe streaking and an effective defocusing of the image because of the uncertainty introduced in the beam position. This is apparently a recurrent problem, because the same difficulty arose with pictures taken in April. Attempts to locate the cause of the problem failed because the oscillation disappeared as soon as the investigation began.

Testing the film recorder for resolution consisted of playing back a specially prepared digital tape through the digital recording system. The test pattern is divided into five horizontal bands, each about 15 mm high; the top, middle, and bottom bands each consist of a sequence of black-and-white bars of variable spacing, suitable for scanning by a microdensitometer to determine resolution. The other two bands have identical gray scales, each consisting of eight rectangles about 13 mm wide. Digital inputs for these eight rectangles are 2, 4, 8, 16, 32, 64, 128, and 255.

The resolution-band black bars (on the print) correspond to a digital input of 0, and the white bars to an input of 180. The highest spatial frequency in the top and bottom bands occurs at the edges, whereas in the middle band it occurs at the center. This highest frequency consists of one black line and one white line, each one spot wide, thus occupying 2/4096 of the film width. The frequencies from highest to lowest are 20, 10, 5, 2.5, 1.25, 0.625, 0.312, and 0.156 cycles/mm.

Each case tested required defining a modulation-transfer function (MTF) using the definition

$$MTF(i) \frac{N_{xi} - N_{0i}}{N_{xi} + N_{0i}}$$

where i = spatial frequency

N_{xi} = the digital input number corresponding to the peak density observed frequency i

N_{0i} = the digital input number corresponding to the minimum density observed at frequency i

N_{xi} and N_{0i} can be derived from a microdensitometer trace of the spatial pattern and the gray scale.

Before beginning each resolution test, the density of each step of the gray scale required adjustment to a specified level because the computed MTF is a function of the gray-scale density curve. For example, it is possible to improve the MTF without alteration of the CRT, the lens, or the film, by adjusting the film recorder to produce a higher density for middle-range signals without changing the maximum or minimum density. However, if the film exposure is changed (for instance, by changing the lens opening), this merely shifts the density (transmission) curve left or right and does not affect the MTF. To avoid apparent changes in MTF caused by changes in the gray-scale curve from test to test, the gray scale of test 1 was selected as the standard. Figure 18 shows this gray-scale density curve, which exhibits excellent linearity. Test 1 represents the present status of the film recorder operating in closed loop with the lens wide open (f/56) and a spot duration of 3.5 microseconds. Under these conditions, the spatial frequency at which the MTF equals 50 percent is 6 cycles/mm. This is better than that of the color-film recorder at Rosman (4.9 cycles/mm), probably because of manufacturing variations or engineering improvements in the size of the CRT spot.

Table 1 summarizes the results of other tests that compared the effect of closed and open loop, change in lens aperture, changes in spot duration, and the use of yellow filters to reduce the blue components of the CRT light output.

Computation of the relative beam current defined the beam current of test 1 as 1.00 and used the pulsewidth and density data:

$$\text{Relative beam current} = \left(\frac{3.5}{p}\right)\left(\frac{f}{5.6}\right)^2\left(\frac{E}{T}\right)$$

where

- p = pulsewidth
- f = f-stop of the lens
- E = exposure ratio (<1), found from the change in density between test 1 and any other test by using Figure 18
- T = transmission factor ($T = 1.00$ with no filter, and 0.65 with filter 8 or filter 15)

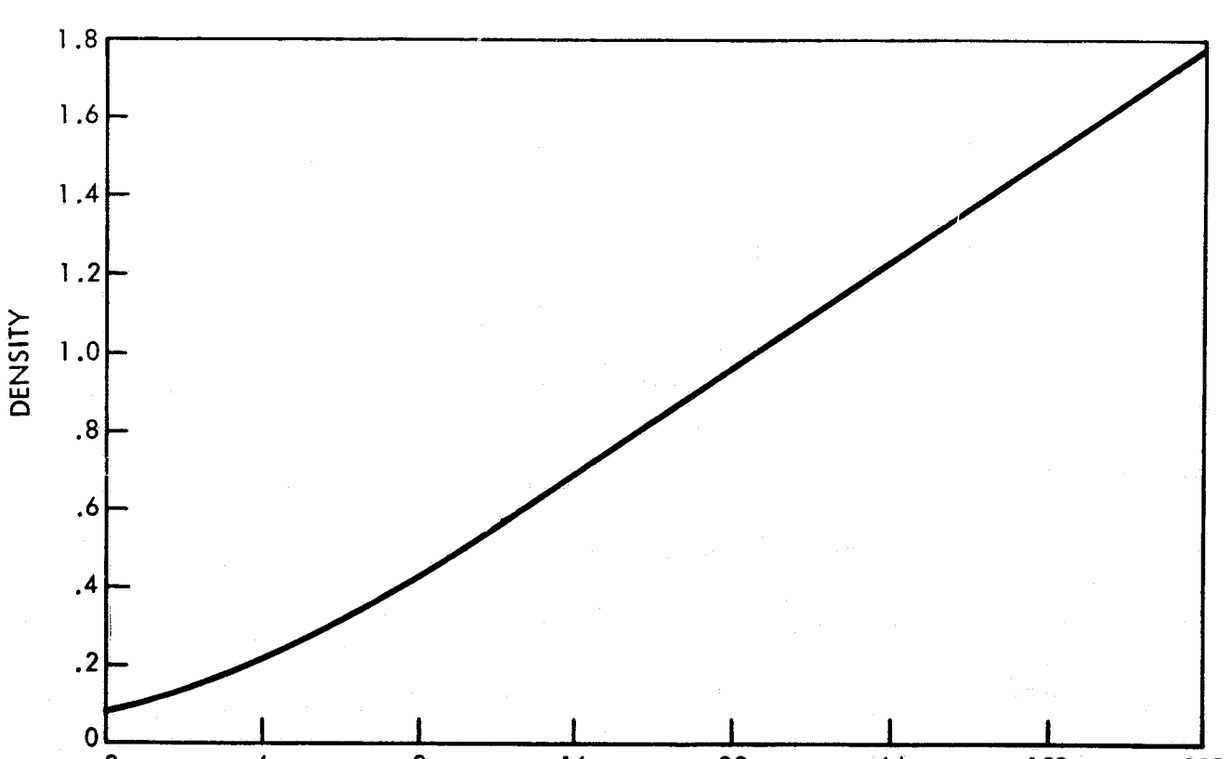

Figure 18. Gray-Scale Density Curve

Table 1

Resolution Test Results

Test	Loop	Pulse-width (p) (μsec)	(f) Lens	Filter	D max - D min	Relative Beam Current	Spatial Frequency at 50% MTF (cy/mm)	
							Center	Corner
1	Closed	3.5	5.6	None	1.74	1.00	6.0	3.3
2	Open	3.5	5.6	None	1.36	0.36	4.2	
3	Open	18	5.6	None	1.52	0.10	3.6	—
4	Open	18	5.6	8	1.52	0.14	4.8	—
5	Open	18	8	None	1.42	0.17	5.9	—
6	Open	40	11	None	1.46	0.17	8.0	5.6
7	Open	40	5.6	15	1.55	0.07	5.2	—

In test 5, for example, relative beam current $= \frac{3.5}{18}\left(\frac{8}{5.6}\right)^2 \frac{0.43}{1.00} = 0.17.$

The significance of these results appears more clearly in Figure 19, a plot of resolution versus relative beam current. The five tests at f/5.6 provide resolutions near 4.8 cycles/mm. Probably the most important result is the improvement of resolution with decrease in lens aperture; at a beam current of about 0.17, the resolution increases from 4.6 cycles/mm at f/5.6 to 5.9 cycles/mm at f/8, to 8.0 cycles/mm at f/11.

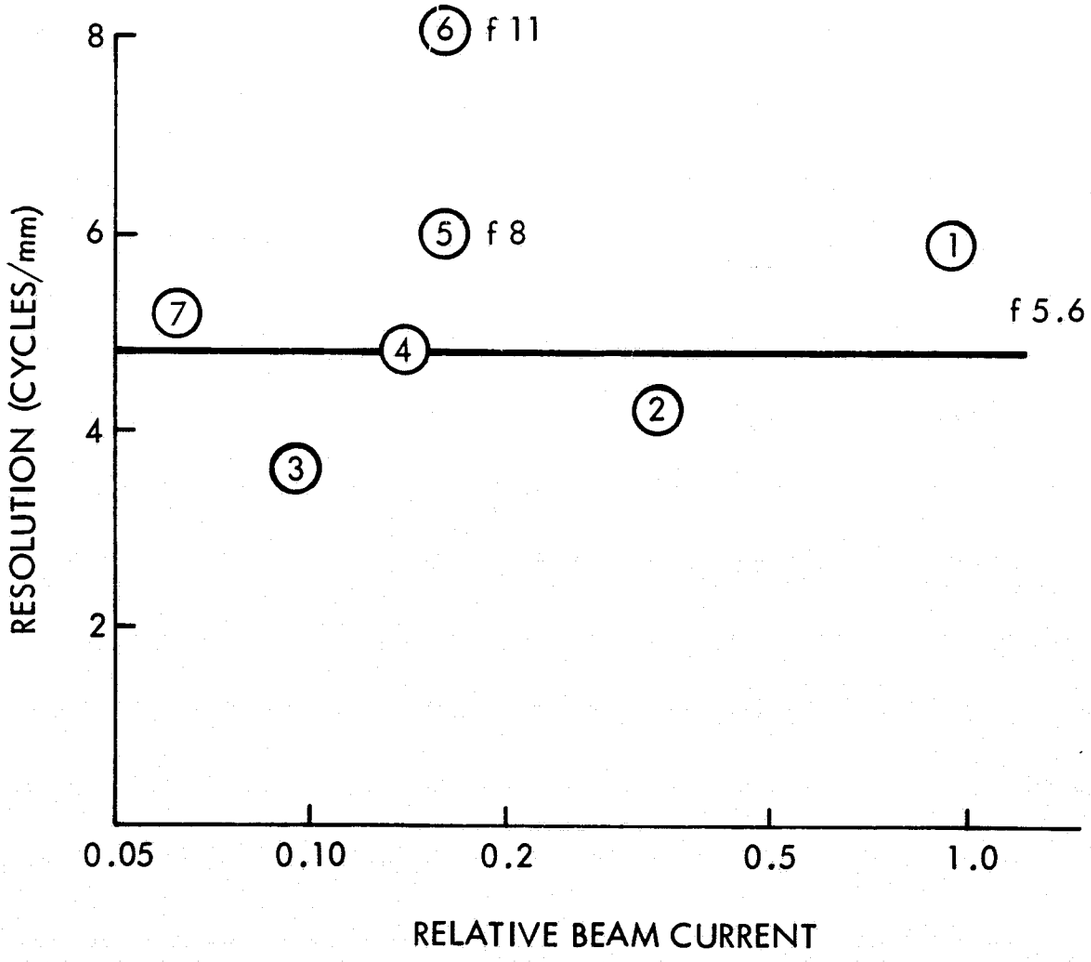

Figure 19. Resolution vs Relative Beam Current

Furthermore, the corner resolution for the f/11 test (number 6) was 70 percent that of the center, compared to an f/5.6 test (number 1) in which the corner resolution was only 56 percent that of the center. These results indicate that growth of the CRT spot diameter with increased beam current is not noticeable in the range tested, and that performance increases substantially with a decrease

in lens aperture. The improvement is probably the result of fewer lens aberrations and increased depth of focus; film sag may present a problem. Use of yellow filters did not improve performance in the cases tested.

Tests to check uniformity of exposure in both open and closed loop exposed a piece of 55 P/N film at one-quarter input (64) across the entire raster. Each negative was scanned with a microdensitometer along the top, bottom, and sides from left to right, noting the density at ten equally spaced points along each scan. In both the open and the closed loop, maximum density was reached along the center scan. The closed-loop case showed an average density decrease for the top and bottom scans of 0.038 and 0.031 respectively, and of 0.010 and 0.065 for the open-loop case. No individual density reading in the closed-loop case varied more than 0.05 from the average; of the thirty open-loop readings, four exceeded this limit. No individual reading in any case varied more than 0.06 from the average.

Therefore, although variations in density were slightly less for the closed loop than for the open loop, both were smaller than the density variations resulting from photographic processing.

Raster width and height measured in inches were 3.995 (±0.010) and 3.072 (±0.008). Linearity was thus excellent (better than 0.3 percent). This size is larger than that of the Rosman raster, and requires a smaller enlargement ratio to provide the same size final print as from negatives generated at Rosman.

Line-to-line spacing on the film recorder should be 1.536 times the spot-to-spot spacing. For a measured raster of 3.995 inches (4096 spots and 2048 lines), the proper height would be 3.065 inches; thus the measured height of the raster is too high by about 0.2 percent.

DIGITAL RECORDING SUBSYSTEM PERFORMANCE

The data on performance of the SSCC digital recording subsystem at Mojave were taken when the subsystem was located at Rosman, and before addition of the real-time buffer and expanded playback modifications. However, they are representative of subsystem performance, which has been generally satisfactory.

Results of the performance tests indicate that the encoded data are correctly time-buffered through core storage and properly formatted and read out to the photofax and digital-tape units. Signature data are being correctly loaded and attached to the front end of line data. Analysis of results reveals proper encoding of analog data and, except for some smaller effects described in subsequent paragraphs, the analog-digital calibration seems adequate and the distribution of digital-data values in line with what is expected from the input data.

Analysis of ramp test data shows a small difference in quantization between positive-going and negative-going signals. A plot of analog input versus digital output should be a linear staircase function, the width (analog change) of each step being approximately equal to the analog equivalent of a 1-bit digital change. Although a positive-going ramp yielded this result, the step width for negative-going ramps was equivalent to a 2-bit digital change. The problem appears to lie in the area of the least significant bit, and results from a peculiarity of the A/D converter with no great impact on the quality of the encoded data.

Recent tapes of earth pictures show occasional sharp changes in the video signal for single samples of a line; the number of changes is not large enough to change the quality of photofax records or digital recordings, but they do show up in enlargements of photofax records. This problem seems to originate in noise from the video data during quantization.

The digital-tape unit seems to perform well both as regards tape-transport operation and as regards quality of data. Transport operation, which reflects the mechanical and pneumatic condition of the unit, should remain satisfactory as long as proper preventive maintenance continues. Preventive maintenance also helps reduce tape-data errors, because it prevents a buildup of tape particles to the point of distorting or obstructing proper tape motion.

Few indications of tape error have appeared in the playback of tapes at Westinghouse; normally, no more than a few records per reel contain errors, and these have been mostly parity errors. Conditions representing loss of characters on the tape, or leading to improper line size, line count, or data readout, have been few. Occasionally, data records appear broken, and this results in single record errors in the line count.

Although the use of thin 1-mil tape causes apparent errors and nonrepeatable results during playback from some users, this type of tape has produced few errors during playback at Westinghouse and the results have been repeatable. Use of 1-mil tape is necessary in order to store full data frames on a single reel of standard-length tape. Extended length reels are needed for use of 1.5-mil tape. Use of high-quality tape seems to result in fewer errors; Westinghouse playback of pictures recorded on Ampex 1-mil tape, for instance, has provided results that are repeatable and nearly error-free.

As an example of digital recording subsystem performance, take the analysis of a single frame of data acquired June 15, 1967 (day 166), at 2142 GMT. This particular tape was generated after all significant system problems at the Rosman ATS site had been corrected. The signature data for ground and satellite gain were in error, but were subsequently corrected.

The tape contained 1990 records, the first at line-count 32 and the last at line-count 2021. (The first-line count at 32 was the result of a late start by the operator.) The tape does not include time record because the SDS-910 program was not turned on; however, previous tests showed that the time recording at Rosman was operating properly.

Scan mode and direction were both zero, indicating normal mode and north-south scan. The frame identifier was arbitrarily set to 1, and the day was set to 166.

The phase-lock loop error was negative to begin with, reaching a maximum negative value of -15 at line-count 50. Maximum positive value reached was +7. Computed average sync error was -2.8, and the computed rms-sync error was 3.2.

Video-data content was apparently satisfactory: of about 16×10^6 video samples, only 66 (about -.004 percent) were at or above the maximum encoding level of 255. This actual video can serve to check on the A/D calibration, using sample values 4 to 43, a set that includes about 46 percent of all the samples and is reasonably uniform in distribution. With perfect calibration, the odd sample values (5, 7, 9, . . . 43) should occur as often as the even values (4, 6, . . . 42). Only 40 percent of these values are in fact odd-numbered, whereas 60 percent are even-numbered. This difference probably results from the dominance of the even values on negative-going data, noted in the previous description of the ramp tests.

The test just described checks the least significant bit; checking the third least significant bit required grouping the data by the state of this bit, which is equal to 1 in type 1 data.* Type 2 has this bit equal to 0. Type 1 sample values between 4 and 43 should occur as often as those of type 2 (i. e., values from 4 to 43 that exclude type 1). In fact, type 1 occurs 49.3 percent of the time, compared to 50.7 percent for type 2. This evaluation indicates a uniform distribution of the data, showing that the A/D errors were confined largely to the least significant bit.

Reviewing the distribution of sample-to-sample differences provides further information on operation of the A/D encoder system. Analysis of camera response to a black-and-white edge indicated that, at most, the sample-to-sample change would not exceed about 0.36 of full scale, or $0.36 \times 255 = 92$. The data apparently meet this condition.

*Type 1 values are 4, 5, 6, 7, 12, 13, 14, 15, 20, 21, 22, 23, 28, 29, 30, 31, 36, 37, 38, 39.

Use of the system at Rosman revealed several problems affecting the quantizing and handling of video data, and led to changes that improved the results achieved with photofax records and magnetic-tape recordings.

Early tape recording upon analysis displayed a tendency toward high-amplitude values in the data scale and a large amount of noise in the data. Westinghouse personnel at Rosman found that the external digitize command pulse to the A/D converter (the mark-in pulse) contained ringing on the trailing edge, causing two consecutive encoding processes with an insufficient time interval. This resulted not only in excessive data values, but also in considerable variation (noise) in the digital values. Changing the circuit at the termination of the line to the converter produced the proper shape for the mark-in pulse; also, the readout pulse for the converter (mark-out pulse) was delayed 1 μs to provide more settling time for the digital-data lines of the converter. The changes made use of available digital circuitry in the digital recording system. The result was a significant reduction in amplitude error.

This correction led to detection of another problem in the quantizing process--erroneous half-scale and quarter-scale positive outputs. Although at first these errors seemed to occur at higher data frequencies (above 5 kHz), further investigation showed that they occurred at all frequencies above approximately 50 Hz. Increasing the size of a capacitor in the sampler and the level output amplifier circuits for the two most significant bits of the A/D converter unit corrected the problem; analysis of subsequent test tapes indicated absence of these errors.

Another problem was that playback of data to the photofax equipment required more settling before read-in than had been expected. Changing the digital recording system to delay the data-strobe pulse to the photofax equipment by 1 microsecond proved particularly helpful for the low-order data bits, because of the manner of loading data into the playback-output register of the digital recording system.

Analysis of test tapes using ramp inputs to the A/D converter showed a reversal in position of the odd and even data samples; this fault was not discernible in the photofax records. The problem was related to another problem observed earlier: the last signature value was affecting the second sample value (now identified as the first sample value). The difficulty arose from improper use of the A/D converter-output strobe for clocking sample data into a 16-bit buffer before loading them into core storage. The addition of an inverter circuit to delay clocking from leading edge to trailing edge of the strobe corrected the reversal of data and the signature crosstalk. Analysis of subsequent test tapes verified the absence of these problems.

For a brief period just before shipping the system to the Mojave site, test tapes and data tapes revealed an error in the 2^3 bit of the A/D converter. An open condition in the cable caused the 2^3 bit to be interpreted as constantly ON. Replacement of the cable corrected this condition.

The system setup at Mojave included a modification to correct failure to sense end-of-file in the playback mode, and to correct an error in signature data input. A small change in the logic served to sense end-of-file marks on the tape, and addition of circuits solved a problem of interfacing with the synchronizer for signature-data inputs of satellite-video gain and ground-video gain.

Although the Datamec D2020 tape unit operated satisfactorily during its original use at Rosman, the solution of problems in other areas together with accumulated experience in using the unit directed attention to tape-transport problems affecting both the transport and the tape itself. The record and reproduce electronics had given no indication of unsatisfactory operation.

On two separate occasions, a tape snag developed around the forward-drive capstan; the tape became wound around the capstan and applied excess force to the forward-drive actuator assembly, causing damage not correctible in the field. The actuator units required repair by the tape-unit manufacturer. Investigation of the two malfunctions and of the tape-transport operation revealed no specific cause for the occurrence but rather a need for regular preventive maintenance, especially as the brand of tape in use at the site caused accumulation of sediment within the transport. To avoid recurrence of the damage, the manufacturer's maintenance instructions were used to set up a procedure for use at the site, and an elapsed-time meter was installed to monitor the operating time of the vacuum-drive portion of the transport, in order to determine proper maintenance schedules. The accumulated operating time of the unit was estimated, and the unit was updated accordingly. The tape-snag problem has not occurred since that time.

APPENDIX A

CALCULATION OF SUN-PULSE SIGNALS

The problem of estimating the position of a single sun pulse is specifically that of estimating the parameter t' from the given signal

$$y(t) = S(t - t') + n(t) \tag{1}$$

The best-known solution to this problem is the linear filter, which produces the maximum-likelihood estimate of t'. Assuming that the additive noise process $n(t)$ is stationary and has a rational spectral-density function, and if the pulse waveform $S(t)$ can be represented by a smooth function having a sufficient number of continuous derivatives, solving for the weighting function and the error variance of the maximum-likelihood filter is not difficult.

Techniques for solving this problem appear in several textbooks, for example that of Davenport and Root.[1] First, obtain the solution $h(t)$ of the integral equation

$$\int_{-T}^{T} R(t - u)\, h(u - v)\, du = \frac{\delta}{\delta v} S(t - v)$$

where $R(t)$ is the autocorrelation function of the noise process $n(t)$ and the integration interval $2T$ is sufficiently large to permit neglecting the end effects (e. g., delta-function terms which appear in the exact solution for $h(t)$).

Next, construct a filter having the weighting function $h(t)$ which will produce in real time the function

$$f(t) = \int_{-T}^{T} h(u - t)\, y(u)\, du$$

$$f(t) = \int_{-T}^{T} h(u-t)\, S(u-t')\, du + \int_{-T}^{T} h(u-t)\, n(u)\, du \tag{2}$$

The maximum-likelihood estimate of the epoch t' is given by the solution $\hat{t}$ of the equation $f(\hat{t}) = 0$. More generally, for a normally distributed estimate of t' with variance u^2, the integration interval of the filter centers on this previous estimate, and the posterior estimate t is the solution of the equation

$$f(\hat{t}) = \hat{t}/u^2 \tag{3}$$

As a simple example, assume a pulse waveform given by

$$S(t) = A \exp\left\{-\frac{t^2}{2\Delta^2}\right\} \tag{4}$$

and white noise with noise-energy N per unit bandwidth. In this case,

$$h(t) = -\frac{1}{N}\frac{\delta}{\delta t} S(t)$$

If the received pulse is actually centered at t', then

$$E\{f(t)\} = \frac{t'-t}{\xi^2} \exp -\left\{\frac{(t'-t)^2}{4\Delta^2}\right\}$$

where $E\{\cdot\}$ denotes the expected value and

$$\xi^2 = \frac{2\Delta N}{A^2 \pi^{1/2}} \tag{5}$$

Note that the slope of $E\{f(t)\}$ at $t = t'$ is given by $-1/\xi^2$, where ξ^2 is the error variance of the single-pulse estimate given by the solution of $f(t) = 0$. The error variance of the posterior estimate which satisfied Equation (3) is

$$\sigma^2 = \frac{1}{\frac{1}{\xi^2} + \frac{1}{u^2}}$$

Figure A-1 is a graph of this solution.

Note the following aspects of this very simple example:

- The general shape of $E\{f(t)\}$, shown in Figure A-1, is typical of more complex problems.
- The slope of $E\{f(t)\}$ at $t = t'$, the epoch at which the received-pulse center actually occurs, is generally expressed by the negative reciprocal of the error variance of the single-pulse estimate.
- The expression shown in (5) for ξ^2 may be written $2\Delta^2 N/S$ where $S = A^2 \Delta \pi^{1/2}$, $\pi^{1/2}$ is the pulse energy, and Δ is proportional to the pulsewidth. If N is the low-frequency noise energy per unit bandwidth, this expression has the form of the general result.

The optimum detector described here is usually difficult to implement, but fortunately some fairly simple detectors exhibit near-optimum performance. For example, in the ATS-B system, the signal $y(t)$ is first prefiltered by a single-pole low-pass filter with an impulse-response function of the form

$$a \exp(-at)$$

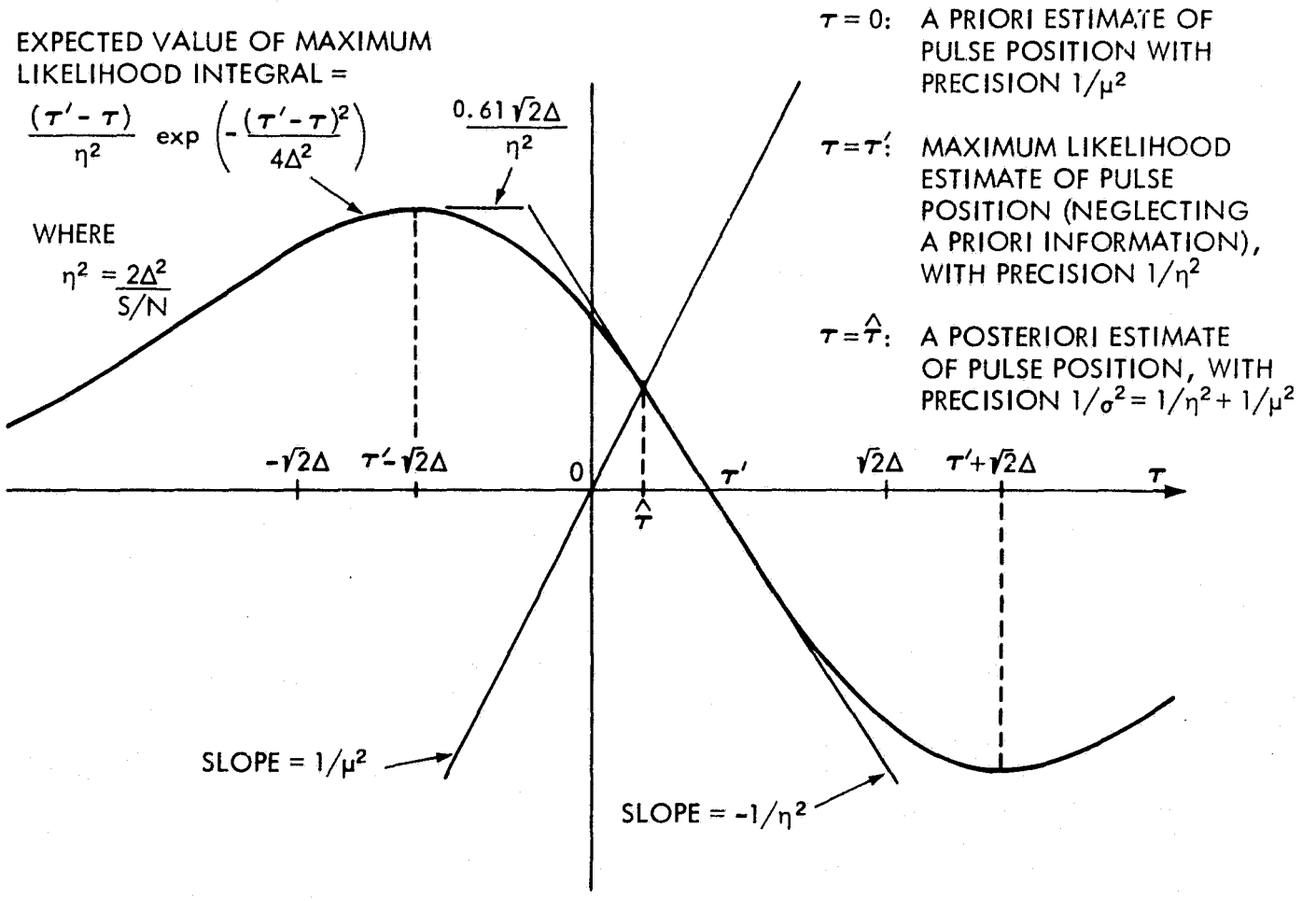

Figure A-1. Expected Value of Maximum-Likelihood Integral

The resulting signal applied to a threshold detector averages the upcrossing and the downcrossing times at the threshold level (Figure A-2).

Let t_a and t_b denote the noise-free upcrossing and downcrossing times, respectively, and let m_a and m_b denote the slopes of the prefiltered pulse at the points t_a and t_b. The estimate of t_a produced by a threshold detector with threshold level L is the value of t for which

$$0 = S(t) + n(t) - L$$

$$= m_a (t - t_a) + n(t)$$

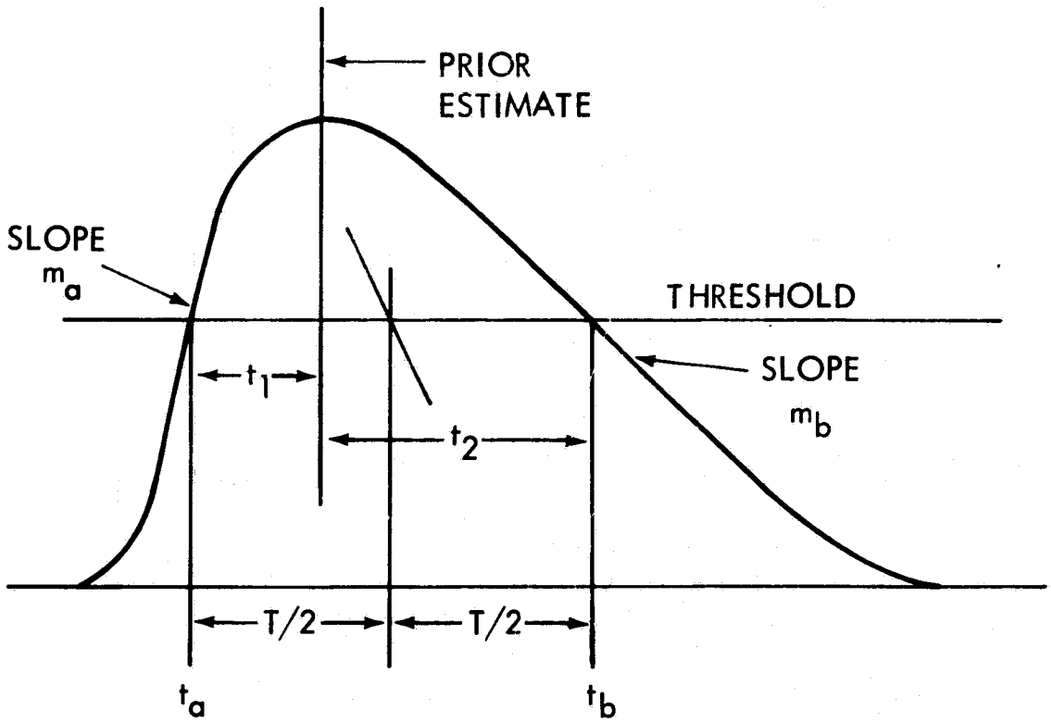

Figure A-2. Threshold Detector

where the foregoing approximation is valid only if the noise variance R(0) is small enough to give the slope of S(t) at the actual upcrossing a high probability of being very nearly equal to m_a. This produces the estimate

$$\hat{t}_a = t_a - \frac{n(t)}{m_a}$$

which has mean value t_a and variance $R(0)/m_a^2$.

Applying a similar argument produces the estimate

$$\widehat{\frac{t_a + t_b}{2}} = \frac{t_a + t_b}{2} - \frac{n(t_a)}{2m_a} + \frac{n(t_b)}{2m_b}$$

which has mean value $(t_a - t_b)/2$ and variance

$$\frac{R(0)}{4m_a^2 m_b^2}\left[m_a^2 + m_b^2 - 2|m_a|\, m_b\, \frac{2(t_a - t_b)}{R(0)}\right] \tag{6}$$

In this expression, the autocorrelation function $R(t)$, the epochs t_a and t_b, and the slopes m_a and m_b are all functions of the prefilter parameter a. If the unfiltered noise has energy density N per unit bandwidth over a frequency range large in comparison to the filter bandwidth, then

$$R(t) = N a \exp(-at) \tag{7}$$

The estimation-error variance (6) also depends on the threshold level L; for a given value of parameter a, the level L should be chosen so that (6) is a minimum. For most reasonable pulse waveforms $S(t)$, the error variance (6) will also have a unique minimum with respect to the filter parameter a.

As an example of the dependence of (6) on the filter parameter, consider again the pulse waveform (4) together with the autocorrelation function of the filtered noise given by (7). Dividing (6) by the optimum error variance ξ^2 given by (5), the resulting expression is independent of the pulse amplitude A and the noise energy N. In fact, the resulting relative error variance depends only on the parameter product $a\Delta$ and the threshold level L.

Figure A-3 illustrates the dependence of the relative error variance on parameter $a\Delta$, where for each value of the parameter the threshold has been adjusted to the optimum level. If system parameters are properly chosen, the error variance of this simple prefilter and threshold detector combination is only 40 percent larger than that of the considerably more complex optimum detector.

One difficulty associated with the threshold detector is that, if the slopes of the leading and trailing edges of the pulse at the threshold level are unequal in magnitude, then a small change in the threshold level (for instance, that produced by a shifting bias) will cause a corresponding change in the nominal pulse center $(t_a + t_b)/2$. Assume that the bias level changes by an amount b sufficiently small to assume that slopes m_a and m_b would remain constant. The shift in the nominal

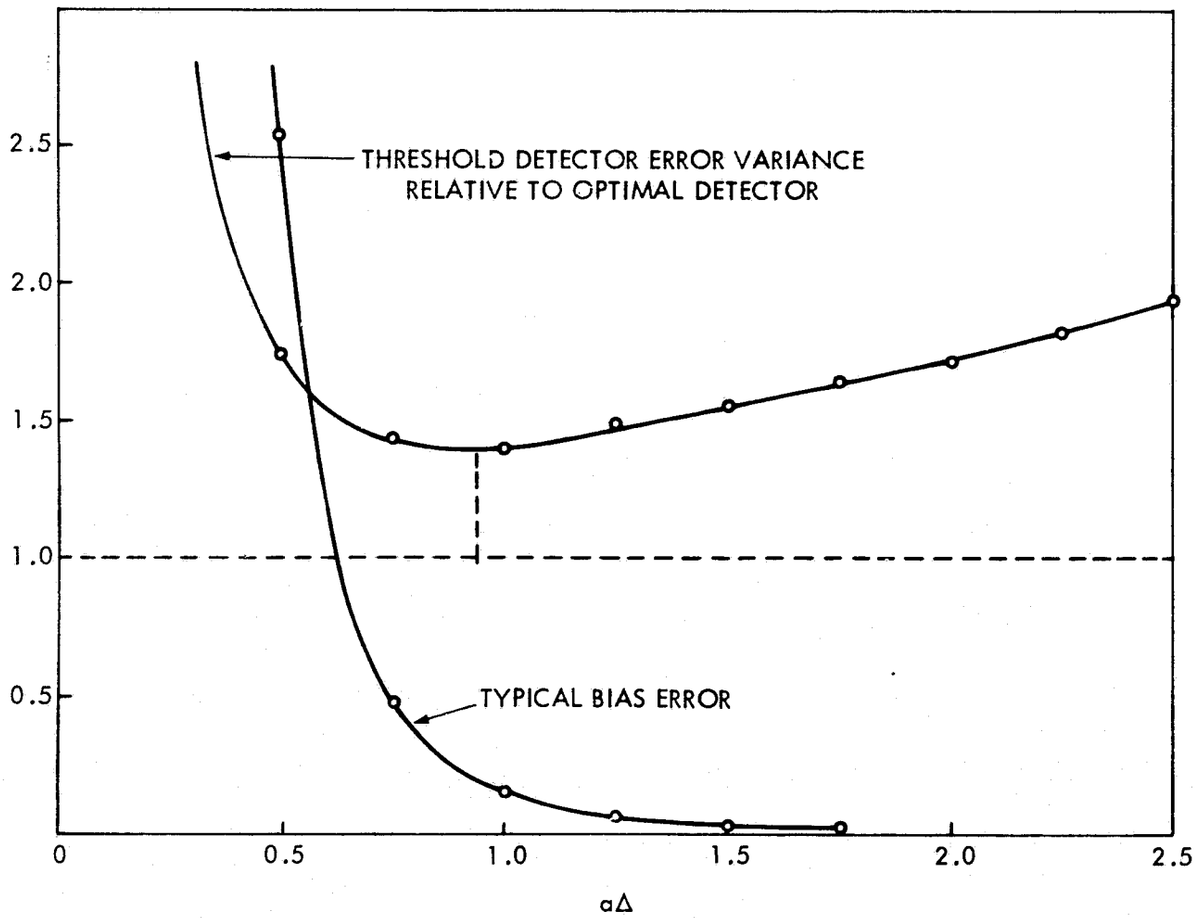

Figure A-3. Threshold-Detector Error Variance Relative to Optimum Detector

pulse center is expressed by

$$\Delta_c = \frac{b}{2} \frac{(|m_b| - |m_a|)}{|m_a\, m_b|}$$

If b is now regarded as a random variable having mean 0 and variance β^2, then the mean-square fluctuation of $(t_a - t_b)/2$ is

$$\frac{(|m_b| - |m_a|)^2}{4 m_a^2\, m_b^2}\, \beta^2 \qquad (8)$$

If, in addition, the random variable b is independent of the other system noise n(t) -- which is nearly always a reasonable assumption -- then the total estimation error variance will be the sum of (6) and (8).

Figure A-3 includes a typical plot of the bias error variance (8) showing the dependence of this quantity on parameter a. For the case shown, $\beta^2/R(0) = 7.1$; it is necessary to rescale this plot for other values of β^2.

In any case, the effect of the random bias error is to increase both the optimum value of the parameter a and the relative variance error of the threshold detector.

The ATS-B system produces an additional error incurred in computing the average $(t_a + t_b)/2$ of the upcrossing and downcrossing times; this is a quantization error resulting from the fact that the average is computed digitally. Let 0 be the previous estimate of the position of an arbitrary pulse, and define

$$\delta = \frac{\text{(estimated interpulse period)}}{294,912}$$

Let n_a denote the integer nearest to $-t_a/\delta$, and n_b the integer nearest to t_b/δ; then the single-pulse estimate generated by the ATS-B detector is given by $(n_b - n_a)\delta/2$. In fact, the actual detector output is the integer $(n_a - n_b)$. The resulting quantization error is triangularly distributed over the interval $(-\delta/2, \delta/2)$ and has variance $\delta^2/24$. (For reference purposes, $\delta^2/24 < 0.2 \times 10^{-12}$ seconds^2.)

The analysis could be repeated in detail for the actual sun-pulse signal and noise spectrum of the ATS-1 system, but the solution is readily deducible. By keeping the bias error at a sufficiently low value and carefully selecting the threshold level and prefilter time constant, the ATS-1 detector should operate with a relative error variance in the range 1.4 to 1.8.

Calculation of Sun-Pulse Dynamic Error

To determine the characteristics of the sun-pulse signals, a digital tape containing about 2000 sampled and quantized sun pulses was recorded. The unavoidable presence of transmission noise and quantization error made it necessary to use a statistical estimate to determine the center-of-gravity of each pulse. The pulses were then aligned and numerically averaged to obtain a typical noise-free sun pulse.

Application of numerical curve-fitting techniques shows that the resulting pulse can be described by the function

$$\left(152.530\,H_0 + 0.063\,H_1 + 2.939\,H_2 - 0.066\,H_3 - 0.613\,H_4\right) \exp\left(-\frac{x^2}{2}\right)$$

where

$$H_0 = 1$$

$$H_1 = 2x$$

$$H_2 = 4x^2 - 2$$

$$H_3 = 8x^3 - 12x$$

$$H_4 = 16x^4 - 48x^2 + 12$$

$$x = \frac{553\,\theta}{\pi} \quad (\text{for } \theta \text{ in radians})$$

Note: The scale factor for this function is 255 for maximum signal input (1.5 volts). The sun pulse therefore had a peak of 0.9 volt and a standard deviation of 0.325 degree. This function fits the numerical data with an rms error of approximately 2 percent.

An attempt to perform a power-spectral density analysis of the typical additive noise in the video signal was unsuccessful because of the extremely small amplitude of this noise. Fortunately, the statistical estimation procedure described here makes it possible to evaluate the performance of the synchronization equipment without relying on the results of the direct-noise analysis.

Let t_k denote the epoch at which the k^{th} sun pulse occurs, and set

$$\Delta k = t_{k+1} - t_k .$$

Then the average angular velocity of the satellite during the k^{th} spin period is $\omega_k = 2\pi/\Delta_k$ radians/second. Setting $d_k = \Delta_{k+1} - \Delta_k$, the average acceleration α_k can be expressed as

$$\alpha_k \triangleq \frac{(\omega_{k+1} - \omega_k)}{(\Delta_{k+1} + \Delta_k)/2}$$

$$= -\frac{\omega_k \omega_{k+1}}{(2\pi)^2} \cdot \frac{2\pi}{(\Delta_{k+1} + \Delta_k)/2} \cdot d_k$$

$$\simeq \frac{\bar{\omega}^3}{(2\pi)^2} d_k , \tag{9}$$

where $\bar{\omega}$ is simply the average of the values ω_k. This approximation holds for the present application because, during a single frame, the extreme values of the set of numbers ω_k differ by only about 5 parts in 10^5. Treating the d_k's as independent identically distributed random variables, with mean $\bar{d}$ and variance δ^2, is essentially equivalent to assuming a random-acceleration model for the satellite spin rate.

Defining vector $x_k^T = (t_k, \Delta_k)$, the dynamic model becomes

$$x_{k+1} = \begin{bmatrix} 1 & 1 \\ 0 & 1 \end{bmatrix} x_k + \begin{bmatrix} 0 \\ 1 \end{bmatrix} d_k \tag{10}$$

The observations (i. e., single-pulse estimates) are of the form

$$y_k = [1, 0]\, x_k + e_k , \tag{11}$$

where the e_k's are independent identically distributed random variables with mean zero and variance η^2. The preceding section gives $\eta^2 = \gamma\xi^2$, where ξ^2 is the error variance of the optimal single-pulse detector and γ is the relative error variance of the actual detector. An excellent discussion of the optimal (linear, minimum-variance) estimation theory associated with the system (10), (11) appears in a paper by Rauch, Tung, and Striebel[2] which contains the details that produce the following results.

Let $\hat{x}(k|n)$ denote the optimal linear estimate of the vector x_k based on the observations $y_1, \ldots y_n$. Also, let $P(k|n)$ denote the covariance matrix of the error vector $\hat{x}(k|n) \triangleq x_k - \hat{x}(k|n)$. The covariance matrices $P(k|k-1)$ and $P(k|k)$ satisfy the following recursive equations:

$$P(k|k-1) = \begin{bmatrix} 1 & 1 \\ 0 & 1 \end{bmatrix} P(k-1|k-1) \begin{bmatrix} 1 & 0 \\ 1 & 1 \end{bmatrix} + \begin{bmatrix} 0 & 0 \\ 0 & \xi^2 \end{bmatrix} \qquad (12a)$$

$$B(k) = P(k|k-1) \begin{bmatrix} 1 \\ 0 \end{bmatrix} \left\{ \left[P(k|k-1) \right]_{11} + \eta^2 \right\}^{-1} ; \qquad (12b)$$

$$P(k|k) = \left\{ I - B(k) \, [1, 0] \right\} P(k|k-1) . \qquad (12c)$$

Starting with an arbitrary initial covariance matrix $P(1|0)$, the three matrices on the left sides of Equations (12a), (12b), and (12c) converge as $k \to \infty$ to steady-state values. Setting $\gamma^2 = \eta^2/\delta^2$, the auxilary parameters u and v are:

$$u = \left[\frac{\left(1 + 16\gamma^2\right)^{1/2} - 1}{2\gamma^2} \right]^{1/2} ;$$

$$v = \frac{(u+2)}{\gamma^2 u^2} .$$

en

$$\underline{\underline{M}} \triangleq \lim_{k\to\infty} P(k|k-1) = \eta^2 \begin{bmatrix} u+v & \\ u & v(u+v)v/(1+u+v)+1/\gamma^2 \end{bmatrix} ; \quad (13a)$$

$$\underline{B} \triangleq \lim_{k\to\infty} K(k) = \frac{1}{(1+u+v)} \begin{bmatrix} u+v \\ v \end{bmatrix} ; \quad (13b)$$

$$\underline{\underline{K}} \triangleq \lim_{k\to\infty} P(k|k) = \frac{\eta^2}{(1+u+v)} \begin{bmatrix} u+v & v \\ v & v(u+v) \end{bmatrix} \quad (13c)$$

Except for the first few lines in a frame, the error variance of the optimal linear estimator very nearly equals these steady-state values. K_{11} may therefore be regarded as the variance of $\hat{t}(k|k)$, the on-line estimate of the epoch t_k; M_{11} may be regarded as the variance of $\hat{t}(k|k-1)$, the one-step prediction of t_k. Figure A-4 illustrates the dependence of the relative variances K_{11}/η^2 and M_{11}/η^2 on the parameter γ^2. To define the lower bound of relative error variances, determined only by extracting all the information from the entire set of single-pulse estimates, Figure A-4 also shows the relative variance resulting from backsmoothing over a doubly infinite sequence of such estimates.

Beginning with the estimate $\hat{x}(1,0)$, the successive values of the on-line estimates $\hat{x}(k|k)$ and the one-step prediction $x(k+1|k)$ are

$$\hat{x}(k|k) = \hat{x}(k|k-1) + B(k)\left\{y_k - [1, 0]\, x(k|k-1)\right\} ; \quad (14a)$$

$$\hat{x}(k+1|k) = \begin{bmatrix} 1 & 1 \\ 0 & 1 \end{bmatrix} \hat{x}(k|k) + \begin{bmatrix} 0 \\ 1 \end{bmatrix} \bar{d} . \quad (14b)$$

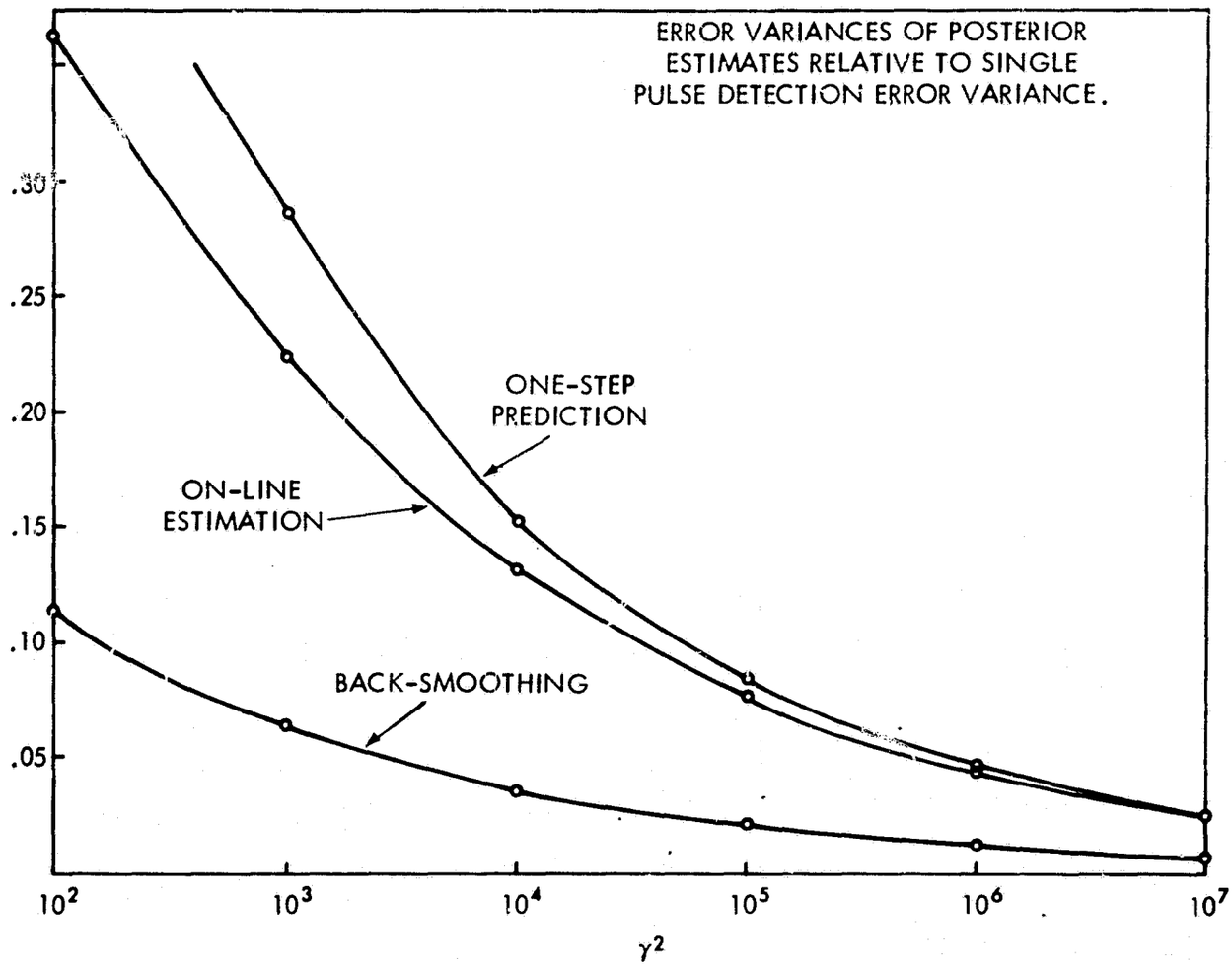

Figure A-4. Error Variances of Posterior Estimates Relative to Single Pulse-Detection Error Variance

Clearly, the optimum linear estimator is more easily implemented by replacing B(k) in (14a) with the steady-state vector B. Components of B depend only on the parameter γ^2, rather than on the separate values of η^2 and δ^2.

The following description of the ATS-B phase-locked loop (PLL), and a discussion of the similarities and differences between this and the optimal linear estimator, will continue to use this notation. For example, $\hat{\Delta}(k|k)$ will now denote the estimate of Δ_k computed by the PLL, so that

$$\delta_k \triangleq \frac{\hat{\Delta}(k|k)}{294,912}$$

Note that δ_k is the value of δ to be used in discussing the quantization error associated with the single-pulse estimate of t_{k+1}. If c_{k+1} is the integer output

of the threshold-detector circuit, and if g_{k+1} denotes the reference time with respect to which this estimate is computed, then the actual single-pulse estimate of t_{k+1} is

$$y_{k+k} = g_{k+1} - c_{k+1}\,\delta_k/2 . \tag{15}$$

The voltage-controlled oscillator (VCO) runs at a frequency $f_k = 1/\delta_k$ during the time that the estimate (15) is being computed. The VCO output applied to a pulse-shaper network results in a pulse train with rate f_k pps that serves as the clock which drives the digital circuitry. This explains why the digital-correction counter that follows the threshold circuit counts once each δ_k seconds during the estimation of t_{k+1}.

The frequency setting of the VCO is determined by the current value, h_k, of an integration counter, which operates as follows: A manually operated switch with switch parameter β can be set at any integer value from 1 through 14 inclusive. After the correction c_{k+1} has been computed, the integration counter is incremented according to the equation

$$h_{k+1} = h_k + 2^{-(14-\beta)}\, c_{k+1} . \tag{16}$$

Letting $\langle r \rangle$ denote the integer part of the real number r, the relation between the VCO frequency and the current value of the integration counter may be expressed as

$$f_k = 2^{-7} \langle 2^7 h_k \rangle . \tag{17}$$

A second switch with parameter α, which has the same settings as the β-switch, is used in conjunction with the β-switch to determine the relative amount of phase correction applied in the PLL. The reference time g_k used by the correction counter is determined by the instant at which another counter (generally

referred to as the sun-angle counter) contains the number zero. At this instant, the sun angle counter is reset to 294,912, and thereafter decremented one count per VCO pulse until the instant g_{k+1} , when the counter once again contains zero. Phase corrections are made by incrementing or decrementing this sun-angle counter by some integer number of counts, which is determined as follows. Setting

$$\ell_k = \langle 2^{(14-\alpha)} h_k \rangle , \tag{18}$$

The sun angle counter is incremented by $(\ell_{k-1} - \ell_k)$ counts at the same time that the correction (18) is made. Therefore,

$$g_{k+1} = g_k - (\ell_k - \ell_{k-1}) \delta_{k-1} + 294,912 \delta_k . \tag{19}$$

Estimates can be expressed as follows:

$$\hat{t}(k|k-1) \triangleq g_k \tag{20}$$

$$\hat{\Delta}(k|k-1) \triangleq \hat{\Delta}(k-1|k-1)$$

$$= 294,912 \delta_{k-1} \tag{21}$$

$$\hat{t}(k|k) \triangleq g_k - (\ell_k - \ell_{k-1}) \delta_{k-1} \tag{22}$$

Therefore, combining (22), (20), (19), (16), and (15) produces

$$\hat{t}(k|k) = \hat{t}(k|k-1) - \left(\ell_k - \ell_{k-1}\right)\delta_{k-1}$$

$$\approx \hat{t}(k|k-1) - 2^{(14-\alpha)}\left(h_k - h_{k-1}\right)\delta_{k-1}$$

$$= \hat{t}(k|k-1) - 2^{-(\alpha-\beta)}\, c_k\, \delta_{k-1}$$

$$= \hat{t}(k|k-1) + 2^{(1+\beta-\alpha)}\left[y_k - \hat{t}(k|k-1)\right]. \qquad (23)$$

Also, using (16), (17), (18), and (22)

$$\hat{\Delta}(k\,k) = 294,912\,\delta_k$$

$$= 294,912\left[\delta_{k-1} + \left(\delta_k - \delta_{k-1}\right)\right]$$

$$= \hat{\Delta}(k|k-1) - \hat{\Delta}(k|k)\left(f_k - f_{k-1}\right)\delta_{k-1}$$

$$\approx \hat{\Delta}(k|k-1) - \hat{\Delta}(k|k)\, 2^{-(14-\beta)}\, c_k\, \delta_{k-1}$$

$$= \hat{\Delta}(k|k-1) + \left[2^{-(13-\beta)}\,\hat{\Delta}(k|k)\right]\left[y_k - \hat{t}(k|k-1)\right]. \qquad (24)$$

Equations (23) and (24), obtained by ignoring quantization effects in the PLL equations, obviously resemble vector Equation (14a) with the vector B(k) replaced by

$$\begin{bmatrix} 2^{(1+\beta-\alpha)} \\ 2^{-(13-\beta)}\hat{\Delta}(k|k) \end{bmatrix} \tag{25}$$

For purposes of analysis, the quantity $\hat{\Delta}(k|k)$ which appears in (25) may be replaced by some average value $\bar{\Delta}$. Substitution is justified because this quantity varies by only about 5 parts in 10^5 during an entire frame.

Using (21) and (22), equation (20) may be re-written in the form

$$\hat{t}(k+1|k) = \hat{t}(k|k) + \hat{\Delta}(k|k) . \tag{26}$$

Equations (21) and (26) are therefore equivalent to the vector Equation (14b) with $\bar{d} = 0$. The PLL thus cannot compensate for the mean deceleration that occurs as the spin-scan camera indexes from the north to the south limit. In steady-state operation, this results in a constant negative bias in the estimates of the epochs t_k.

If the ratio $\gamma^2 = \eta^2/\delta^2$ of the dynamic spin rate model (10), (11) is known, the steady-state vector B of the optimal linear estimator may be computed using Equation (13b) and integer values of α and β can be chosen to minimize the difference between B and the vector (25). The resulting values of α and β may not be optimal, but they do provide an excellent starting point for the optimization procedure.

Consideration of the PLL equations (15) - (19) reveals that, by knowing the initial value of the integration counter h_0, the set of integers $\{c_k\}$, $k = 1, 2, \ldots, N$, and the switch parameters α and β, and by choosing g_1, arbitrarily, then it is possible to reconstruct all other values of interest. In particular, the single-pulse estimates $\{y_k\}$, $k = 1, 2, \ldots, N$, may be obtained in this way. Luckily, the required data is readily available; most of the necessary information appears in the reconstructed data sets $\{y_k\}$.

Suppose that a set of estimates $\{y_k\}$ is processed by a computer-simulated version of either a PLL filter {Equations (15) - (19)} or a filter of the form (14a), (14b). Let $t(k|k-1)$ denote the not necessarily optimal one-step prediction of t_k produced by this filter. The errors $\{t_k - t(k|k-1)\}$ cannot be studied directly because there is no way to determine the exact values of the epochs t_k; however, it is possible to investigate the differences $\{y_k - t(k|k-1)\}$. Equation (12) produces

$$y_k - t(k|k-1) = e_k + [t_k - t(k|k-1)]$$

where e_k is statistically independent of the term in square brackets. Hence,

$$\text{Var}\{y_k - t(k|k-1)\} = \eta^2 + \text{Var}\{t_k - t(k|k-1)\} \quad (27)$$

Furthermore, because of the ergodic nature of the differences $\{y_k - t(k|k-1)\}$, once a steady state has been reached the sample variance of the tail of this sequence represents a good estimate of variance (27).

Therefore, processing the same data set $\{y_k\}$ through several versions of the PPL filter (corresponding to different values of the α and β parameters) will produce a fairly accurate map of the variance (27) considered as a function on the $\alpha - \beta$ lattice. This makes it possible to determine the optimum settings of the α and β switches for this particular data set. Repeating this process for a number of data sets $\{y_k\}$ will reveal the values of α and β that give the best average performance.

The main drawback to the above procedure is that it offers very little information on either the model parameters or the estimation errors. Using the linear minimum-variance filters makes the situation quite different, because almost a complete analysis is available for these equations. This case uses a simulation of the steady-state version of the estimation Equations (14a), (14b) to search for the minimum of the variance (27) with respect to the filter parameter γ^2. Figure A-5 shows a typical example of the dependence of this variance of γ^2. The simulated data set used in this example demonstrates that the minimum occurs at the value of γ^2, which corresponds to the variances used in the data model. Estimates of $\text{Var}\{y_k - t(k|k)\}$ plotted here show that this function is not very useful for parameter estimation.

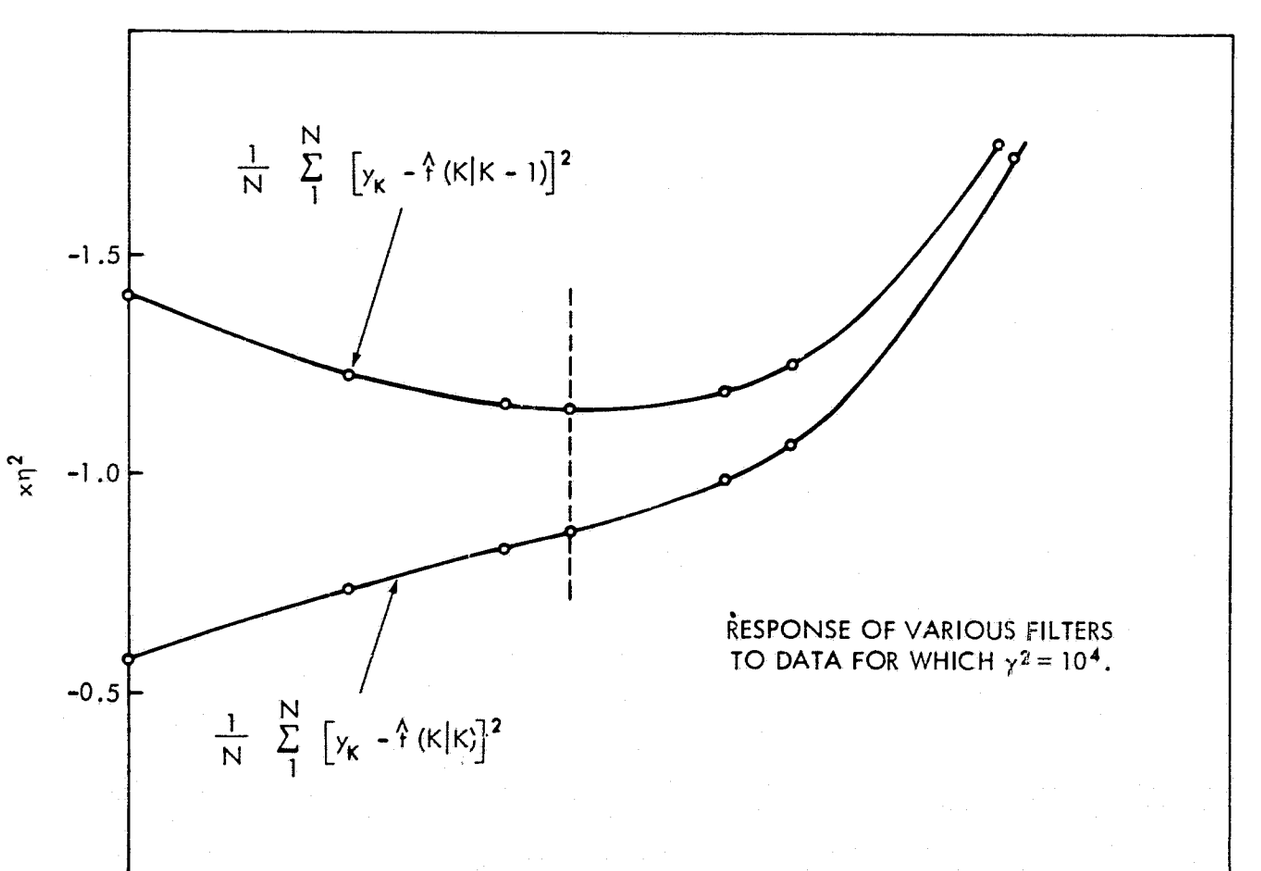

Figure A-5. Response of Various Filters to Data for Which $\gamma^2 = 10^4$

If the data set is reasonably well described by a system of equations of the form (10), (11), (12) then all linear optimal filter theory discussed in the preceding section is applicable at the minimum point, so that

$$\mathrm{Var}\left\{y_k - t(k|k-1)\right\} = \eta^2 + K_{11}$$

$$= \eta^2 \left(1 + K_{11}/\eta^2\right),$$

or

$$\eta^2 = \frac{\mathrm{Var}\{y_k - \hat{t}(k|k-1)\}}{(1 + K_{11}/\eta^2)} \quad . \tag{28}$$

Knowing the minimizing value of γ^2 can enable calculation of the value of K_{11}/η^2 from Figure A-5. This produces an estimate of the variance η^2, and therefore also of $\sigma^2 = \eta^2/\gamma^2$.

As the estimation Equation (14b) is linear in the parameter $\bar{d}$, $\hat{t}(k|k-1)$ can be expressed for each k in the form

$$\hat{t}(k|k-1) \triangleq \hat{t}_p(k|k-1) + \hat{t}_q(k|k-1)\,d \; .$$

Hence, for some value of $\bar{d}$ and some positive integer m, the expression

$$\frac{1}{(M-m)} \sum_{m+1}^{N} \left[y_k - \hat{t}_p(k|k-1) - \hat{t}_q(k|k-1)\,\bar{d}\right]^2 \tag{29}$$

may be used as an estimate of the variance (27). In fact, taking the minimum value of the righthand side of (29) with respect to $\bar{d}$ as an estimate of $\mathrm{Var}\{y_k - \hat{t}(k|k-1)\}$ produces the estimate

$$\bar{d} = \frac{\sum \hat{t}_q(k|k-1)\left[y_k - \hat{t}_p(k|k-1)\right]}{\sum \hat{t}_q^2(k|k-1)} \tag{30}$$

Hence, by assuming that a model of the form (10), (11) is appropriate for a particular data set $\{y_k\}$, it is possible to set up procedure for estimating the values of the model parameters which apparently best describe that data set. Adjusting either the threshold level or the prefilter time constant of the pulse detector, and then studying the resulting estimates of the detection error variance η^2, enables calculation of the optimal settings for these parameters. Furthermore, after obtaining an estimate of the variance (27) for the optimal PLL filter, it is possible to subtract from this quantity the estimated value of ^{2} for that data set, and thereby obtain an estimate of the one-step prediction-error variance.

Optimum Filter/PLL Comparison

To evaluate the performance of the PLL (including the effects of time and frequency quantization) and to compare this performance with that of the optimum second-order filter described in the preceding section, it was necessary to simulate the PLL.

If a pulse arrives at time t_c, with upcrossing and downcrossing times t_1 and t_2 respectively, and if the early/late gate transition is set at G, then the correction counter counts up for a time $\langle G - t_1 \rangle$ that provides a number of counts $\langle (G - t_1) F \rangle$ in which F is the current VCO frequency and $\langle\ \rangle$ denotes the integer part. Similarly, the countdown is given by $\langle (t_2 - G) F \rangle$. Therefore the number left in the correction counter is

$$C = \langle (G - t_1) F \rangle - \langle (t_2 - G) F \rangle \tag{31}$$

The error or time difference E between the pulse center and the gate is

$$E = G - t_c \tag{32}$$

where $t_c = (t_1 + t_2)/2$

Therefore

$$E = \left[(G - t_1) - (t_2 - G) \right] / 2 \tag{33}$$

or

$$E = C\,2F \tag{34}$$

ignoring the effects of time quantization.

If the gate is late, then the number in the correction counter will be positive; conversely, if the gate occurs before the pulse center, the correction-count number will be negative.

This correction count is then used to control the digital integrator: that is, if correction count is positive, then as the counter counts down to zero the digital integrator counts up the same number of counts. If the count is negative, the integrator will be reduced by the same number of counts. This number of counts is added to or subtracted from the integrator at a point controlled by the β parameter or frequency-correction switch (S37). Therefore, the number in the integrator after the correction application is given by:

$$I_k = I_{k-1} + \beta C_k \tag{35}$$

where

$$\beta = 2^{(S37-14)} \tag{36}$$

The frequency synthesizer then uses the integrator to generate a new basic clock frequency; the new VCO frequency is the same as the number in the integrator, out to the seven most significant bits of the fractional part of the integrator number:

$$F_k = \langle 2^7 I_k \rangle / 2^7 \tag{37}$$

where F_k is the VCO frequency.

The phase correction uses a fractional part of the frequency correction to advance or retard the sun-angle counter by either adding or deleting VCO clock pulses. This phase correction P_k is actually a function of the difference between the integrator contents before and after the addition of the latest correction count.

$$P_k = \langle \alpha I_k/\beta \rangle - \langle \alpha I_{k-1}/\beta \rangle \tag{38}$$

where $\alpha = 2^{(S37-S38)}$. Therefore

$$P_k = \langle 2^{(14-S38)} I_k \rangle - \langle 2^{(14-S38)} I_{k-1} \rangle \tag{39}$$

The sun-angle counter merely counts the VCO clock pulses along with the addition or deletion caused by the phase correction, until it reaches a predetermined number M at which time the gate is generated for the correction counter. The time of this gate is thus

$$G_k = G_{k-1} + (M - P_k)/F_k \tag{40}$$

Rewriting Equation 31 with the proper subscripts yields:

$$C_k = \langle (G_{k-1} - t_{1k}) F_{k-1} \rangle - \langle (t_{2k} - G_{k-1}) F_{k-1} \rangle \tag{41}$$

Equations 35 through 41 thus provide a mathematical description of the PLL.

The occurrence of the smooth sun pulse or gate is employed to present the earth-angle counter to the corrected beta count, and also to advance the earth-angle counter by the VCO clock pulses generated by the frequency synthesizer.

The earth-angle counter then generates most of the timing pulses of the synchronizer, including line start, line end, execute enable, and the dc-restore gate. It also provides outputs to the azimuth generator and the fiducial-mark generator of the subtiming system, as well as to the sync error display.

The PLL analysis consists of simulating the PLL operation on a digital computer. Figure A-6 is a flow diagram of this simulation. The purpose of the dynamic model block is to generate a series of sun-pulse times which closely approximates the actual pulse sequences obtained from experimental data. Timing of the pulses can be approximated by

$$t_k = t_{k-1} + \Delta_{k-1} \tag{42}$$

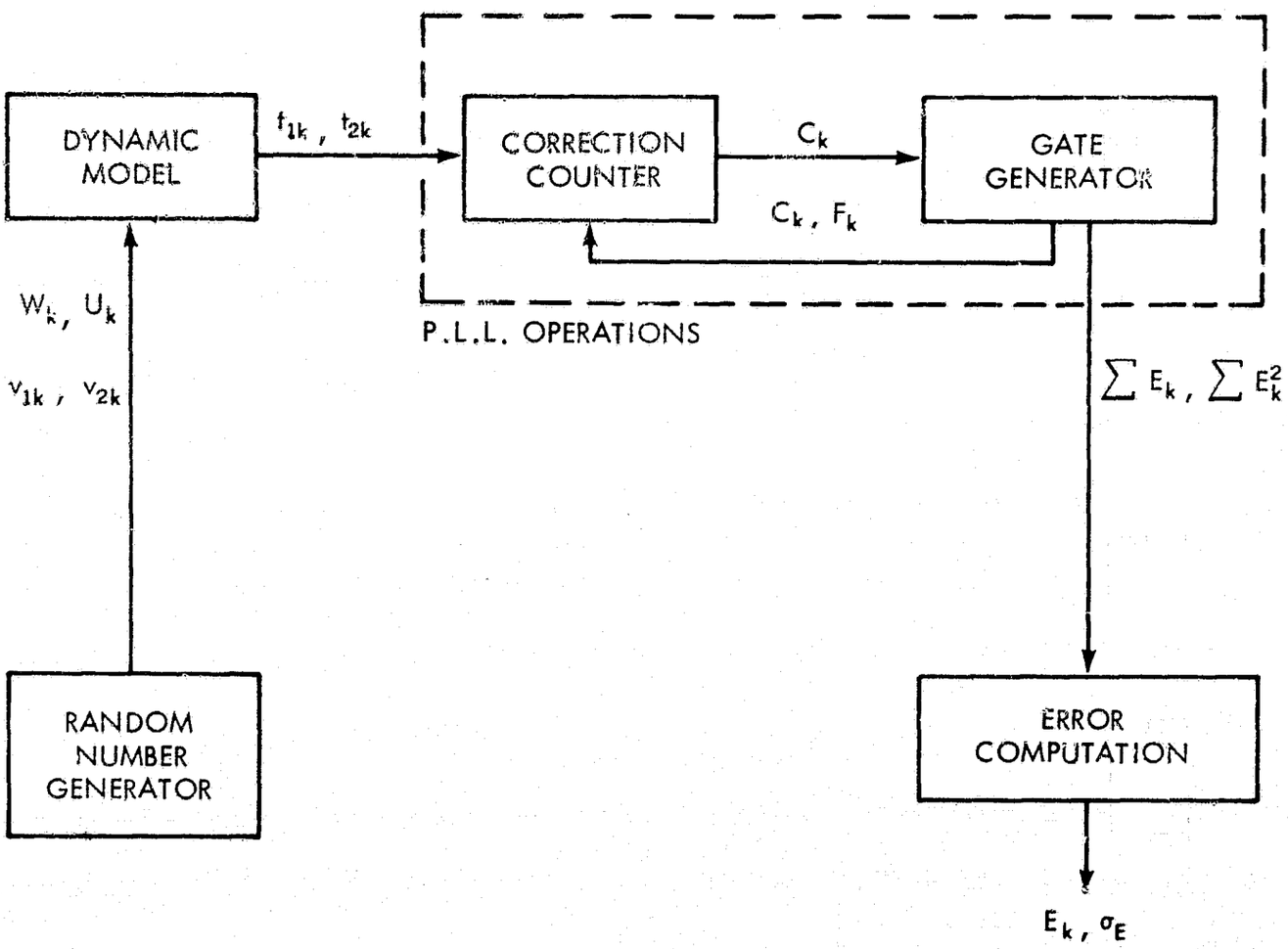

Figure A-6. Phase-Lock Loop Simulation Flow Diagram

$$\Delta_k = \Delta_{k-1} + U_{k-1} \tag{43}$$

where t_k is the time of occurrence of the k^{th} sun pulse center, Δ_k is the first-order timed difference, and U_k is a normally distributed random variable with mean $\bar{U}$ and variance δ^2.

Times actually used in the PLL operation are those associated with the threshold crossings, defined as

$$t_{1k} = t_k + \mu_{k1} - W_k \tag{44}$$

$$t_{2k} = t_k + d + \mu_{k2} + W_k \tag{45}$$

where d is the pulsewidth, W_k is a uniformly distributed random variable that accounts for the variation in pulsewidth due to time quantization, and μ_{k1}, μ_{k2} are the normally distributed variables with zero mean and variance N^2 that define the measurement errors at the threshold points.

The initial value for Δ_k is given by

$$\Delta_0 = \frac{M}{f_0} . \tag{46}$$

and arbitrary values are selected for f_0, t_0, and d.

Random variables W_k, μ_{k1}, μ_{k2} and U_k are provided by the random-number generator. First, three random numbers r_{1k}, r_{2k}, and r_{3k}, uniformly distributed over [0, 1], are generated from an existing subroutine. New variables X_k and Y_k are formed:

$$X_k = 2r_{1k} - 1 \tag{47}$$

$$Y_k = 2r_{2k} - 1 \tag{48}$$

If $X_k^2 + Y_k^2 > 1$, then the larger of the two values r_{1k}, r_{2k} is rejected and a new value for it is obtained, until $X_k^2 + Y_k^2 \leq 1$.

Then

$$Z_k = \frac{\left(-2\ln r_{3k}\right)^{1/2}}{X_k^2 + Y_k^2} \tag{49}$$

and

$$a_j = \left(X_k^2 - Y_k^2\right) Z_k \tag{50}$$

$$b_j = 2X_k Y_k Z_k \tag{51}$$

where a_k and b_k are two independent normally distributed random variables with zero mean and a variance of 1.

Then

$$U_k = U + \delta a_k \tag{52}$$

where U and δ^2 are the mean and variance, respectively, associated with uncertainties in satellite spin motion. Actual values for these parameters are determined from data available elsewhere in the study.

Using the same routine and three new variables r_{4k}, r_{5k}, r_{6k}, another pair of variables c_k, d_k is computed corresponding to a_k, b_k. These variables are then used to calculate the measurement inaccuracies:

$$\nu_{1k} = \left[2\left(N^2 - \delta^2/24\right)\right]^{1/2} C_k \tag{23}$$

$$\nu_{2k} = \left[2\left(N^2 - \delta^2/24\right)\right]^{1/2} d_k \tag{54}$$

$$\delta = \frac{1}{f} \tag{55}$$

where f is the nominal frequency and $\delta^2/24$ is the measurement variance associated with the time quantization.

The random variable that accounts for the pulsewidth variations can be expressed by the uniformly distributed variable:

$$W_k = \frac{\delta}{2\sqrt{24}} r_{7k} \tag{56}$$

All these calculations offer ways of obtaining realistic sets of threshold times corresponding to each k^{th} sun pulse.

The pulse times are then fed to the PLL correction counter along with the previously generated gate or smoothed sun-pulse estimate.

The difference in time along with the current VCO frequency gives the correction count

$$C_k = \langle (G_{k-1} - t_{1k}) F_{k-1} \rangle - \langle (t_{2k} - G_{k-1}) F_{k-1} \rangle \tag{57}$$

that can be used to compute a new gate:

$$I_k = I_{k-1} + 2^{(S37-14)} C_k \tag{58}$$

$$F_k = \langle 2 I_k^7 \rangle / 2^7 \tag{59}$$

$$P_k = \langle 2^{(14-S38)} I_k \rangle - \langle 2^{(140S38)} I_{k-1} \rangle \tag{60}$$

$$G_k = G_{k-1} + (M - P_k)/F_k \tag{61}$$

At the same time, the new sync error computed as

$$E_k = \frac{C_k}{2F_k}$$

is used to update a running sum of the errors and a running sum of the squares. The gate generator also requires inputs for the phase and frequency-switch settings S37 and S38, previously calculated parameters I_{k-1} and G_{k-1}, and of course initial conditions for I_0 and G_0:

$$I_0 = f_0 \tag{62}$$

If the initial value for (t_0) is chosen as $(-\Delta_0)$ so that

$$t_0 \approx 0 \tag{63}$$

then

$$G_0 = \frac{C_1}{2f_0} + \frac{d}{2} \tag{64}$$

where C_1 is the desired correction count for $k = 1$.

The sum of the sync errors and the sum of the square of the sync errors serve to calculate a mean sync error and variance for $k = N$.

$$\bar{E}_k = \frac{1}{(N-125)} \sum_{k=126}^{N} E_k \tag{65}$$

$$\sigma_E^2 = \frac{1}{(N-125)} \sum_{k=126}^{N} E_k^2 - (\bar{E}_k)^2 \tag{66}$$

In order to eliminate the transients, the first 125 sets of sync errors were not used in the mean and variance computation.

The data sets $\{r_k\}$ used in estimating both the threshold-detector measurement errors and the parameters of the stochastic spin-rate model came from various digital tapes: for example, tapes 136B, 137A, 137B, and 137C contain digital records of earth pictures recorded under normal operating procedures at the Rosman site on days 136 and 137.

Tapes 282, 283, 284, and 285, which contain earth pictures recorded at the Mojave site, are the result of a special series of threshold-level tests. Approximate sunpulse width in ms at the threshold level for each of these four tapes is

Tape	Sun-Pulse Width
282	1.4
283	1.6
284	1.2
285	1.0

Similarly, tapes TH-1, TH-2 and TH-3 are part of a series of threshold tests at Rosman. As this threshold series is incomplete, the special nature of these tapes will be ignored.

Finally, this study includes the results of a test tape generated by passing a sequence of simulated pulses from a stable source, (rather than actual sun sensor pulses) through the threshold detector and phase-lock loop. These results demonstrate that the estimation procedure used here is sensitive to parameter values considerably smaller than those associated with the real data sets.

Table A-1 lists estimated values of the mean second difference $\bar{d}$, the variance δ^2 of the second differences, the single-pulse detection-error variance η^2, and the ratio R between error variance (27) produced by the linear minimum-variance filter and that produced by the phase-lock loop filter. As variance (27) appears to be a usable figure for evaluating system performance, it is especially interesting to note that the phase-lock loop performs about as well as the optimal linear filter.

With regard to the Mojave threshold series, note that tape 282, corresponding to a pulsewidth of 1.4 ms at threshold level, produces the minimum value of the detection-error variance η^2. Also note that the detection errors are somewhat larger at Mojave than at Rosman, probably because of a higher system-noise level at the Mojave site.

Table A-2 lists several values of variance (27) for each of the data sets. The first value is that obtained by passing the actual data through the PLL filter (i. e., the variance produced by the operating system); the second is that produced by passing the actual data through the linear minimum-variance filter found to be optimal for that data set. Next, the parameter values given in Table A-1 served to generate a simulated data set. The third and fourth values listed in Table A-2 for each data set result from passing simulated data through the simulated PLL

Table A-1

Parameter Estimates

Tape No.	$10^8 \bar{d}$	$10^{12} \eta^2$	$10^{16}\ \delta^2$	R
137A	1.274	7.978	0.468	1.004
137B	1.592	5.248	230.39	0.353
137C	1.460	6.119	0.133	0.998
136B	1.445	8.948	0.0678	1.039
282	1.388	14.934	0.147	1.018
283	1.362	15.686	0.265	1.040
284	1.383	16.958	3.442	1.024
285	1.319	17.999	0.417	1.035
TH-1	1.384	19.560	1.319	0.987
TH-2	1.440	10.689	0.192	0.998
TH-3	1.591	10.268	0.371	1.016
TEST	-0.00034	1.110	0.0019	1.061

filter and the simulated linear filter respectively. The purpose of these results was to determine whether or not data generated by the stochastic model compared favorably with actual system data; the results amply justify the choice of model.

After eliminating the parameter values in Table A-1 associated with the test tape plus a few other extreme values, averaging the remaining parameters produces the following typical values:

$$\bar{d} = 1.4 \times 10^{-8} \text{ sec}$$

$$\delta^2 = 0.64 \times 10^{-16} \text{ sec}^2$$

$$\eta^2 = 9 \times 10^{-12} \text{ sec}^2 \quad \text{(Rosman)}$$

$$\eta^2 = 16 \times 10^{-12} \text{ sec}^2 \quad \text{(Mojave)}$$

Table A-2

Comparison of Simulated and Real Data

Tape No.	Real Data, PLL Filter	Real Data, MV Filter	Simulated Data, PLL Filter	Simulated Data, MV Filter
137A	0.083	0.083	0.085	0.087
137B	0.214	0.076	0.433	0.087
137C	0.065	0.065	0.071	0.070
136B	0.090	0.093	0.102	0.105
282	0.153	0.156	0.152	0.152
283	0.159	0.165	0.177	0.173
284	0.183	0.186	0.180	0.181
285	0.184	0.190	0.202	0.193
TH-1	0.213	0.210	0.217	0.218
TH-2	0.115	0.114	0.121	0.123
TH-3	0.107	0.109	0.113	0.113
TEST	0.0108	0.0114	0.0134	0.0119

Data sets based on these typical parameter values were passed through the simulated PLL filter for various settings of the α and β parameters. In each case, the value of variance (27) was computed to determine which values of α and β produced the smallest value of this variance.

Tables A-3 through A-6 shows the results of these tests. Tables A-3 and A-4 are associated with the value $\eta^2 = 9 \times 10^{-12}$ sec^2 which is typical for Rosman; these results require setting $\beta = 5$ or 6, and $\alpha = \beta + 5$. Tables A-5 and A-6 show that the best switch settings for the Mojave site are $\beta = 6$ and $\alpha = \beta + 5$.

Table A-3

Determination of Optimum Switch Settings for $\eta^2 = 9 \times 10^{-12}$ (Case 1)

β/α	8	9	10	11	12
4	0.990	0.982	1.016	1.359	—
5	—	0.966	0.955	1.034	1.475
6	—	1.028	0.957	0.951	1.047
7	—	—	1.002	0.977	1.005

Table A-4

Determination of Optimum Switch Settings for $\eta^2 = 9 \times 10^{-12}$ (Case 2)

β/α	8	9	10	11	12
4	1.091	1.057	1.093	1.247	—
5	—	1.095	<u>1.049</u>	1.085	1.363
6	—	1.140	1.071	1.072	1.126
7	—	—	1.148	1.090	1.113

Table A-5

Determination of Optimum Switch Settings for $\eta^2 = 16 \times 10^{-12}$ (Case 1)

β/α	8	9	10	11	12
4	1.668	1.655	1.691	2.084	—
5	1.976	1.853	<u>1.818</u>	1.876	2.155
6	—	1.972	1.877	1.846	1.938
7	—	—	1.991	1.894	1.927

Table A-6

Determination of Optimum Switch Settings for $\eta^2 = 16 \times 10^{-12}$ (Case 2)

β/α	8	9	10	11	12
4	1.869	1.832	1.845	1.998	—
5	1.976	1.853	<u>1.818</u>	1.876	2.155
6	—	1.972	1.877	1.846	1.938
7	—	—	1.991	1.894	1.927

Direct Sun-Pulse Optimization

This series of tests was to experimentally determine the optimum threshold level (producing minimum time jitter on the detected sun pulse) for the sun-pulse detector in the synchronizer, by plotting PLL performance vs sun-pulse width and noting the point of maximum PLL performance. The parameter for measuring PLL performance is the standard deviation of the sync-error distribution obtained from the digital tapes; the lower the value of this number, the better the PLL performance. Because the PLL's transient response to rapid spin-rate changes during camera retrace causes large sync errors (and therefore contributes largely to the variance, which tends to mask the contributions of the region of interest), the variance calculation was based on data from line 75 to line 2000. This also eliminates the effect of late starts in the digital recording system. The sun-pulse threshold level was measured in terms of sun pulsewidth because operationally it is the width, and not the level, which is adjusted. Also, if the sun-pulse shape does not change, the seasonal changes of sun-pulse amplitude is compensated for, if the width rather than a threshold level is used to set the threshold detector.

Figure A-7 is a plot of sync-error variance vs sun-pulse width. The performance of the Rosman PLL is slightly better than that of the Mojave PLL, probably because of the higher signal-to-noise ratio at the Rosman station. Minima of both curves occur at approximately the same sun-pulse width, 1.4 ms, which is the optimum value for operation with ATS-B.

$\alpha + \beta$ Optimization

After optimizing the sun-pulse threshold level came a series of tests to determine the optimum values of α (the phase-correction rate) and β (the frequency-correction rate) for the PLL when operating with the ATS-B spacecraft. The optimum value of the two PLL constants is that which corresponds to the minimum sync-error variance. The variance calculation is again based on the data from line 75 to 2000 for the reasons given previously. Table A-7 shows the results of a computer analysis of the nine α and β tapes.

Whereas the table shows that the minimum observed value of the variance occurred for $\alpha = 11$ and $\beta = 8$, Figure A-8 (a plot of the standard deviation of the sync error as a function of α and β) does not indicate a trend towards this minimum value. In either case, the points in question occur at the edge of the data field; before any clear recommendation can be made, more data covering a larger data field must be taken. Although the data field is too small to clearly define a minimum, it does show that the value of the function does not change appreciably over the data field, and therefore the selection of $\alpha + \beta$ may not be as critical as once thought.

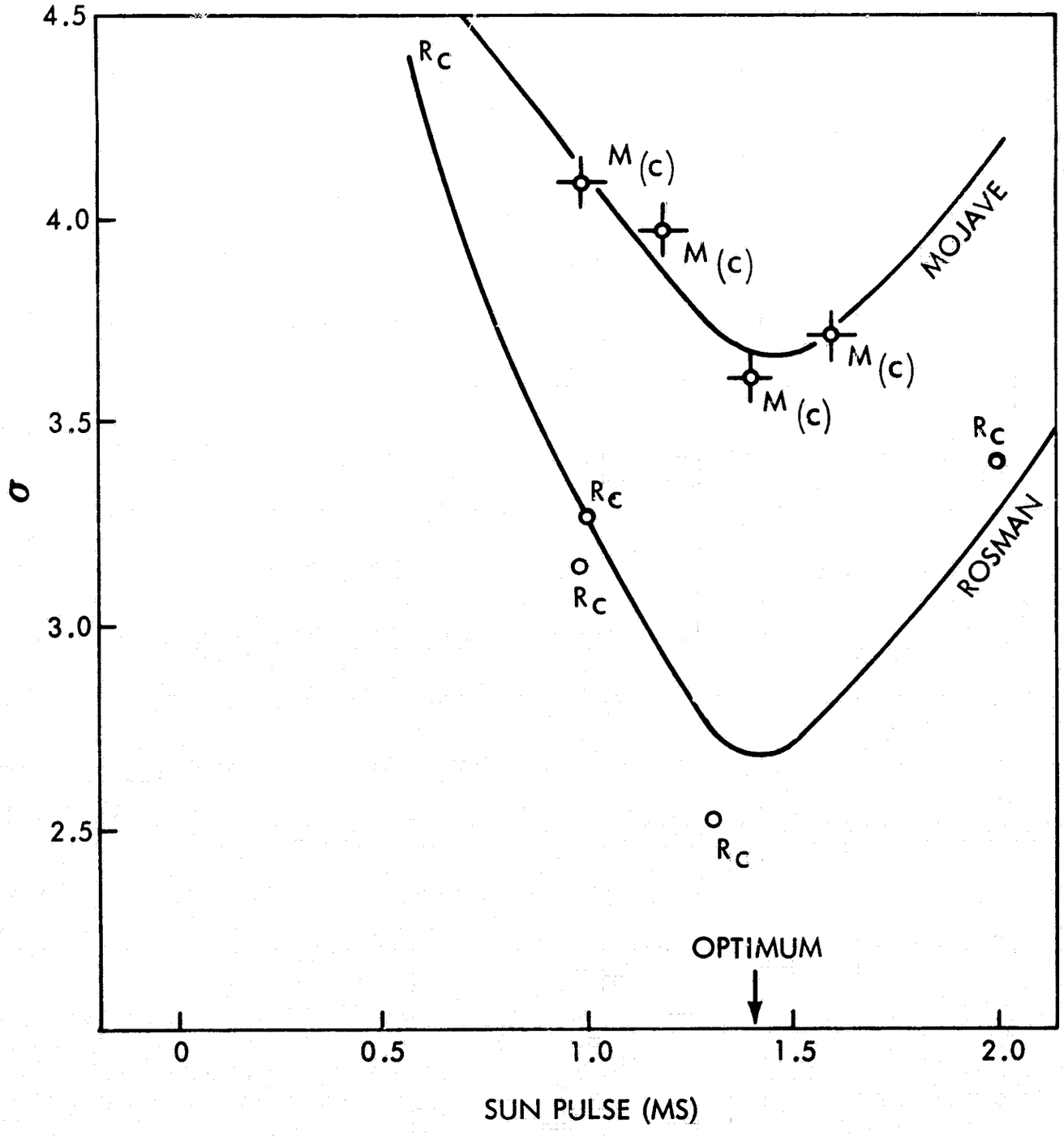

Figure A-7. Threshold Test

Additive Noise and Acceleration Effects

Repeated attempts to perform power spectral density analysis of additive noise in the video and sun pulse have produced only questionable results. An indirect method, described fully in PLLE, has determined the effect of this additive noise. The method was to construct an input-time sequence of sun pulses using the sync error from a SSCC digital tape and introduce this input into a optimum linear

Table A-7

Sync Error Mean and Variance

Tape	α	β	$\bar{X}$	σ^2
1	11	7	-1.54	22.11
2	10	6	-2.80	17.80
3	9	5	-5.43	23.09
4	11	5	-5.96	24.06
5	11	8	- .93	9.90
6	9	6	-2.49	11.59
7	10	5	-5.90	16.09
8	10	7	-2.93	18.38
9	11	6	-2.37	20.74

filter. As the parameters of this filter can be uniquely described in terms of the noise variance and spin acceleration variance, it was possible to adjust these parameters until optimum filtering occurred and then compute the required variances.

Average input time variation (standard deviation) was 3 microseconds for Rosman and 4 microseconds for Mojave.

The standard deviation of the spin acceleration is 0.8×10^{-8}/second^2. This latter number may be converted to radians/sec^2 by multiplying by $2\pi/\tau^3$ where τ is the nominal spin period. $2\pi/\tau^3 = 29$. Thus the rms spin acceleration is about 0.23 microradian/sec^2. The mean spin acceleration is $1.4 \times 29 \times 10^{-8} = 0.4$ microradian/sec^2.

Effectiveness of the PLL

Results of the sun-pulse dynamic model can help to determine the actual PLL error, which is the time difference between the PLL output and the true sun-pulse center (no noise). The PLLE states that

$$\gamma^2 = \frac{\eta^2}{\delta^2}$$

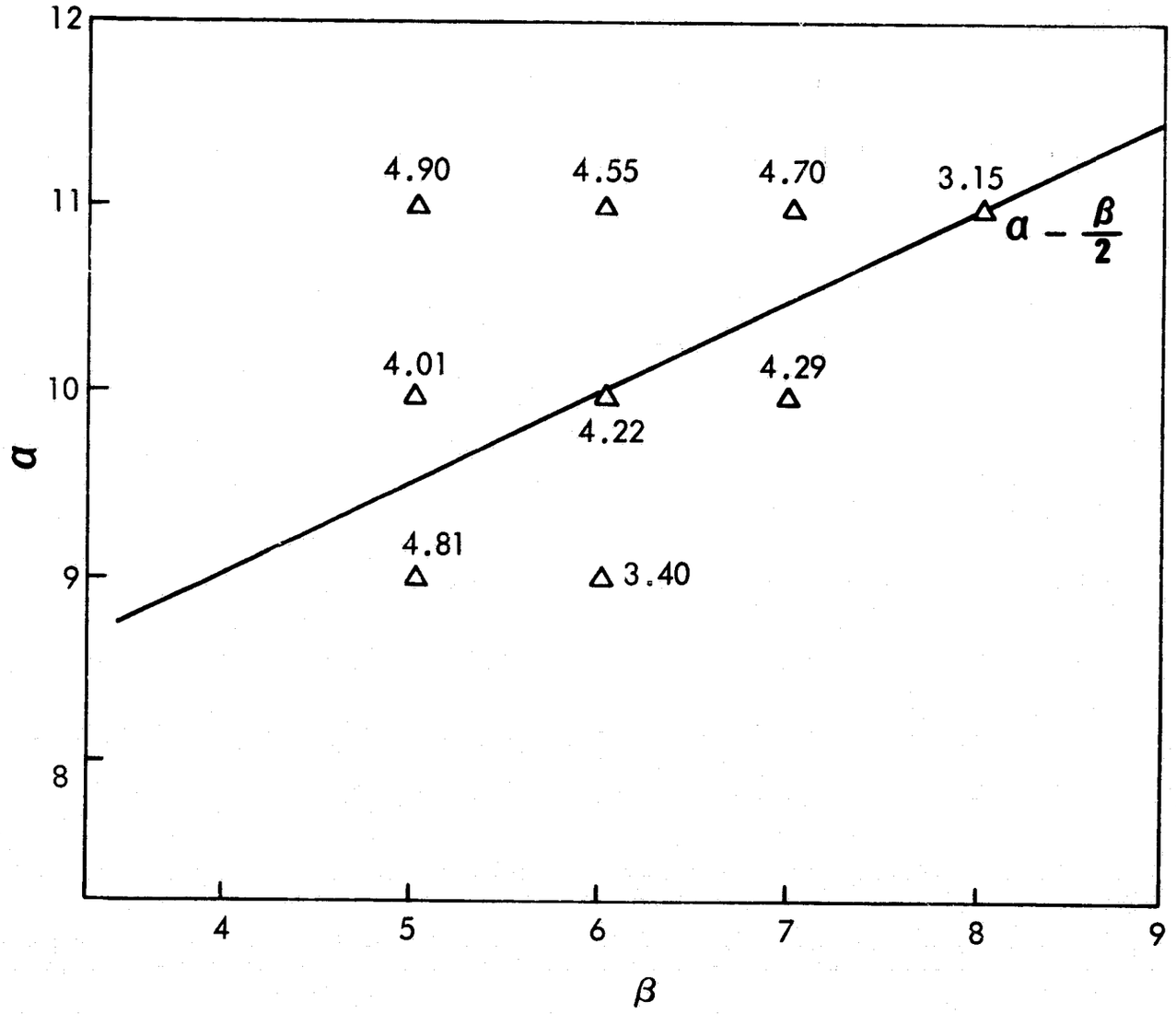

Figure A-8. $\alpha + \beta$ Optimization

$$\gamma_R^2 = \frac{9 \times 10^{-12}}{.64 \times 10^{-16}} = 1.4 \times 10^5 \quad \text{(Rosman)}$$

thus

$$\gamma_M^2 = \frac{16 \times 10^{-12}}{.64 \times 10^{-16}} = 2.5 \times 10^5 \quad \text{(Mojave)}$$

Figure A-4, using the one-step prediction error curve, shows that the PLL at Rosman provides a variance-reduction factor of 0.076, an RMS-reduction factor

of approximately 0.28. For Rosman, the PLL RMS error is therefore

$$0.28 \times 3.0 = 0.84 \quad \text{microseconds}$$

Similarly, the PLL at Mojave provides a variance-reduction factor of 0.063, or an RMS-reduction factor of approximately 0.255. Hence, the PLL RMS error at Mojave is

$$0.255 \times 4.0 = 1.02 \quad \text{microseconds}$$

Estimation Errors

One method of estimating probable errors associated with the foregoing numbers is to run a controlled test with little added noise or spin acceleration. Results of such a test, run with the system built-in test sequence, indicate a time jitter at the output of the threshold detector of less than 1.1 microseconds, and an rms spin acceleration of less than 0.025 microradians/sec^2. The indicated mean acceleration is less than 0.0002 microradians/sec^2. The estimation procedures used are apparently sensitive to parameter values considerably smaller than those found for the PLL.

Note that the 1.1-microsecond jitter at the output of the threshold detector includes a time-quantization jitter of about 0.4 microsecond.

SOURCES

1. Davenport, W. B. and W. L. Root, An Introduction to the Theory of Random Signals and Noise, McGraw-Hill Book Co., New York (1958)

2. Rauch, H. E., F. Tung and C. T. Striebel. "Maximum Likelihood of Linear Dynamic Systems." AIAA Journal, III, 8. (August 1965). pp. 1445-50

APPENDIX B

CALCULATION OF THE EFFECT OF THE PREEMPHASIS NETWORK ON LOW-FREQUENCY SPACECRAFT RESPONSE

Shortly after operations with the ATS spacecraft began, a preemphasis network was installed between the receiver-modification amplifier in the Mojave ground-station equipment used for the spin-scan cloudcover camera and the video-processor input, in order to correct for insufficient low-frequency response in the spacecraft. The signal droop caused by the spacecraft electronics for a given video signal was computed, and the effect of the preemphasis network was checked using step and frequency-response methods. Finally, the effect of the preemphasis network on a typical spacecraft signal was checked.

The spacecraft electronics was specified to have a low-frequency response expressed as

$$\frac{S^2}{(S + 2\pi f_1)(S + 2\pi f_2)}$$

where $f_1 = 0.234$ Hz and $f_2 = 1.12$ Hz.

A video pulse 28.4 ms wide (corresponding to 20 degrees of sweep by a satellite having a 512-rms spin period) was used for comparison. Under these conditions the video would droop by 21.8 percent.

The preemphasis network has a low-frequency response expressed as

$$\frac{S(S + 2\pi f_1)(S + 2\pi f_2)}{(S + 2\pi f_3)^3}$$

where $f_3 = 0.07$ Hz.

The net effect of the spacecraft and preemphasis electronics was a droop of about 3.8 percent, which means that the preemphasis network should account for a boost of 18.0 percent. Actual measurements of this unit at Rosman and Mojave

indicate an actual boost of only 16.0 percent; this discrepancy may be due to errors in measurement.

A droop factor may be defined as

$$\frac{\text{(spacecraft droop)} - \text{(preemphasis boost)}}{\text{(spacecraft droop)}}$$

This factor for the measured preemphasis boost is 0.266. For an actual ATS-1 signal without preemphasis, the observed droop was 150 mv; according to these calculations, preemphasis should have reduced this to 150×0.266, or 40 mv. This improvement was in fact noted.

These calculations lead to the following conclusions:

- Low-frequency characteristics of the ATS-1 video are as defined by f_1 and f_2.
- Ground-station preemphasis networks are operating very nearly as designed.
- Redesign of the preemphasis network may reduce the droop factor below 0.266.